

CREEP PERFORMANCE OF A MODIFIED VERSION OF HAYNES 230
PROCESSED WITH LASER POWDER BED FUSION

by
Daniel P. McConville Jr.

A thesis submitted to the Faculty and the Board of Trustees of the Colorado School of Mines in partial fulfillment of the requirements for the degree of Master of Science (Metallurgical and Materials Engineering).

Golden, Colorado

Date _____

Signed: _____

Daniel P. McConville Jr.

Signed: _____

Dr. Jonah Klemm-Toole
Thesis Advisor

Golden, Colorado

Date _____

Signed: _____

Dr. Ivar Reimanis
Professor and Department Head
Metallurgical and Materials Engineering

ABSTRACT

Ni-based superalloys processed by laser beam powder bed fusion (PBF-LB) additive manufacturing (AM) are ideal for the aerospace and power generation industries due to the increased component complexity and part consolidation afforded by AM. However, some alloys exhibit solidification cracking when processed with PBF-LB or may not perform similarly enough to their wrought counterparts. Wide adoption of AM for high temperature structural applications is also restricted, in part, by creep testing and validation. The objective of this project was to assess the creep performance of Haynes 230, a solid solution and carbide precipitate strengthened Ni-based alloy, and compositionally modified forms of the alloy that are crack-free, at 760 °C. The creep life of the modified PBF-LB Haynes 230 is higher than standard PBF-LB Haynes 230 primarily due to increased creep strength resulting from a higher fraction of intragranular carbides. As a result, the creep performance of the modified PBF-LB Haynes 230 is comparable to wrought forms of the alloy. Stress relaxation testing was also explored as a method for high-throughput creep evaluation. It was found that the minimum creep rates determined from stress relaxation testing match well with those derived from conventional creep tests on both standard and modified PBF-LB Haynes 230. It is therefore possible to use stress relaxation testing to more rapidly evaluate creep properties and even as a quality control tool for PBF-LB Ni-based alloys. The findings from these studies suggest that alloys which are considered “unprintable” can be adopted into PBF-LB AM through minor composition and/or microstructure modifications and perform similarly to wrought material. It is also evident that creep data of such materials can be acquired more rapidly with high throughput creep testing. With the implementation of these strategies, there is potential for the development of new alloys and manufacturing methods to be hastened and for the advancement of cleaner energy production.

TABLE OF CONTENTS

ABSTRACT	iii
LIST OF FIGURES.....	vi
LIST OF TABLES	viii
ACKNOWLEDGMENTS.....	ix
CHAPTER 1 INTRODUCTION.....	1
1.1 References	3
CHAPTER 2 BACKGROUND.....	4
2.1 Laser Beam Powder Bed Fusion	4
2.2 Creep	4
2.3 Stress Relaxation Testing.....	5
2.4 References	6
CHAPTER 3 CREEP OF A STANDARD AND MODIFIED VERSION OF LASER POWDER BED FUSION-PROCESSED HAYNES 230	7
3.1 Abstract	7
3.2 Introduction	8
3.3 Methods.....	9
3.3.1 Sample Processing	9
3.3.2 Creep Testing	10
3.3.3 Microstructural Characterization.....	11
3.3.4 Creep Data Analysis.....	12
3.4 Results	13
3.4.1 Microstructure Prior to Creep Testing	13
3.4.2 Creep Results	15
3.4.3 Deformation and Fracture of Creep Specimens	18
3.4.4 Microstructure After Creep Testing	19
3.5 Discussion	22
3.5.1 Contributions to Improved Creep Performance in Modified Ni230	22
3.5.2 Contribution of Microstructural Features to Improved Creep Strength in the Modified Alloy.....	24
3.5.3 Atypical Creep Anisotropy	25
3.5.4 Influence of Crack Elimination on Creep Life.....	25

3.6	Conclusions	26
3.7	Acknowledgments	27
3.8	References	27
CHAPTER 4	STRESS RELAXATION TESTING AS A HIGH THROUGHPUT METHOD FOR ASSESSING CREEP STRENGTH IN LASER POWDER BED FUSION PROCESSED NI-BASED SUPERALLOYS	30
4.1	Abstract	30
4.2	Literature Review and Introduction	31
4.2.1	Characteristics of PBF-LB Haynes 230	31
4.2.2	Motivation for Accelerated Testing	31
4.2.3	Previous Applications of Stress Relaxation Tests.....	32
4.2.4	Objective of This Work.....	32
4.3	Methodology	33
4.3.1	PBF-LB Processing.....	33
4.3.2	Mechanical Testing	34
4.3.3	Microstructural Characterization.....	36
4.4	Results	37
4.4.1	Microstructure in the As-built and Solution Heat Treated Conditions	37
4.4.2	Stress Relaxation Testing.....	39
4.4.3	Microstructure Evolution During Stress Relaxation Testing	42
4.5	Discussion	44
4.5.1	Influence of Starting Strain Upon Loading on Stress Relaxation Tests.....	44
4.5.2	Stress Relaxation Test Sensitivity to Microstructural Evolution	45
4.5.3	Stress Relaxation Test Sensitivity to Differences Between Ni230 and Ni230 TiC ...	46
4.5.4	Ni230 TiC Creep Behavior	46
4.5.5	Considerations for Shorter Stress Relaxation Tests	46
4.6	Summary and Conclusions.....	47
4.7	Acknowledgements	48
4.8	References	49
CHAPTER 5	CONCLUSIONS AND FUTURE WORK.....	52
5.1	Conclusions	52
5.2	Future Work	54
APPENDIX A	PERMISSIONS	56

LIST OF FIGURES

Figure 3.1	Illustration of horizontally and vertically oriented bars, metallography cubes, and a machined creep specimen. Machining dimensions in mm.....	10
Figure 3.2	Optical micrographs of as-built A) standard and B) modified Ni230. EBSD IPF + IQ maps of C) standard and D) modified Ni230, also in the as-built condition. SEM SE micrographs of mixed acids etched E) standard and F) modified Ni230 in the solution heat treated condition. Orientations in the IPF + IQ maps are with respect to the build direction.....	14
Figure 3.3	Creep strain vs. time curves of each alloy at 145, 160, and 190 MPa stresses. Region of interest highlights the tests on standard Haynes 230, which consisted of only XY samples	16
Figure 3.4	Minimum creep rate vs. stress (Norton plot) indicating the creep stress exponent obtained from the three tests on each.	16
Figure 3.5	Stress vs. Larson-Miller parameter comparing standard and modified PBF-LB Ni230 from this work to wrought Haynes 230 [3.20] and PBF-LB Haynes 230 from Wu et al. 2021 [3.8].....	18
Figure 3.6	Comparison of deformation in creep samples of standard Haynes 230 (XY-oriented), modified Haynes 230 (XY-oriented), and modified Haynes 230 (Z-oriented)	19
Figure 3.7	SEM SE micrographs of fracture surfaces of standard XY-oriented, modified XY-oriented, and modified XY-oriented Ni230 from 145 MPa creep tests.....	20
Figure 3.8	EBSD IPF maps of standard XY, modified XY, and modified Z Ni230 just below fracture surfaces from 145 MPa tests illustrating significant differences in creep deformation. IPF coloration is oriented to the vertical direction, which corresponds to the tensile direction of the creep samples.....	21
Figure 3.9	Plots of rupture time vs. stress comparing the influence of A) minimum creep rate B) grain size on the rupture time of standard and modified Ni230. Figure 3.9C shows the influence that the rate at which voids nucleate during creep strain (proportionality constant, α') has on model fit to experimental data.....	23
Figure 4.1	Schematic diagram of the PBF-LB samples on a build plate and the mechanical test specimens	34
Figure 4.2	Light optical micrographs of A) Ni230 and B) Ni230 TiC in the as-built condition. EBSD IPF + IQ maps of C) Ni230 and D) Ni230 TiC in the as-built condition. The build direction and the IPF key is shown on the right of the figures. SEM SE micrographs of E) Ni230 and F) Ni230 TiC in the solution heat treated condition.....	38
Figure 4.3	A) Stress as a function of time for both alloys and two strain conditions each. B) Smoothed stress relaxation curves.	40
Figure 4.4	Creep rate as a function of stress for stress relaxation tests (SRTs) and conventional creep tests (CCTs).	41

Figure 4.5	Minimum creep rate vs. rupture time of Ni230 and Ni230 TiC from conventional creep tests.	41
Figure 4.6	Stress versus Larson Miller Parameter (LMP) for conventional creep tests, 0 % plastic strain stress relaxation tests, and reported Haynes 230 data.	42
Figure 4.7	SEM SE micrographs of A) heat treated Ni230, B) Ni230 post-SRT, C) Heat treated Ni230 TiC, and D) Ni230 TiC post-SRT.	43
Figure 4.8	A) The relaxation observed in the first 24 hours of a stress relaxation test, and B) the range of creep rates assessed as a function of test time	47
Figure A.1	Permission granted by the TMS content department head, Matt Baker, to include the publication of “Stress Relaxation Testing as a High Throughput Method for Assessing Creep Strength in Laser Powder Bed Fusion Processed Ni-based Superalloys” from the proceedings of the Superalloys 2024 conference	55
Figure A.2	Permissions for the use of coauthored materials in this thesis.....	56

LIST OF TABLES

Table 3.1	Composition of Ni230 as reported in the product specification	10
Table 3.2	Microstructure characteristics of standard and modified PBF-LB Haynes 230 in the as-built (AB) and solution heat treated (HT) conditions	15
Table 3.3	Summary of creep data	17
Table 4.1	Composition of Haynes 230 (Ni230) powder used for specimen manufacturing. All values in wt% reported by the powder manufacturer	33
Table 4.2	Creep data from conventional creep tests used for stress relaxation tests	39

ACKNOWLEDGMENTS

I would first like to thank my advisor, Dr. Jonah Klemm-Toole, for his support and guidance throughout this project. The impact that he has had on my academic development over the past two years cannot be overstated.

I also want to thank the folks at Elementum 3D—Ben Rafferty, Stan Baldwin, Kevin Eckes, and Jeremy Iten—for being easy to reach and a pleasure to work with. This work could not have happened without them nor without Dr. Amy Clarke and the Office of Naval Research.

I am grateful to have my family back home consistently encourage me—thank you, mom, dad, Katie, and Ella. I am also fortunate to have friends near and far who keep my spirits up. Thank you, Andrew, Brady, Theo, Finn, and all of my fellow metallurgy graduate students.

CHAPTER 1

INTRODUCTION

Gas turbine engines are widely used for power and propulsion in the modern day. Nearly half of the United States' electrical power is generated by gas turbines [1.1], and they are critical for meeting needs when power demands rise [1.2]. Transportation industries, especially aerospace, have benefitted tremendously from the high efficiency and reliability that gas turbines offer. Additive manufacturing (AM) has the potential to improve these benefits further by enabling more complex designs for improved performance.

Laser beam powder bed fusion (PBF-LB) is an AM technique which can produce complex parts of high spatial resolution by selectively melting and solidifying metal powder. Iron-, nickel-, aluminum-, and titanium-based alloys are the most common alloys processed with the technology [1.3]. Thin layers of metal powder are spread onto a build plate and a high-power laser scans over regions to comprise two-dimensional shapes similar to a conventional printer, causing rapid melting and solidification. This process is repeated with successive layers to generate a three-dimensional part. When excess powder is cleaned away, a complete component remains which may be used as-is or processed further with machining, heat treatments, and/or coatings. Few alloys have been designed specifically for the extreme thermal and residual stress conditions of PBF-LB, so defects can arise when processing materials which have historically been cast or wrought [1.4]. Porosity and cracking are among the most common issues that affect alloys, and these defects are often managed by adjusting the printing parameters, such as the speed and power of the laser scan. Certain alloys may be represented as “unprintable” or “unweldable” if parameter adjustments are insufficient to produce quality parts.

Haynes 230 is one such alloy which exhibits extensive solidification cracking when processed with PBF-LB despite being readily arc weldable [1.5, 1.6]. Solidification cracks throughout the microstructure severely debit the usefulness of parts due to losses in strength and ductility. Cracking can be reduced with parameter optimization, but it is evident that eliminating cracks is insufficient to bring performance metrics up to standard, suggesting that there are additional implications to consider with the fine microstructure that PBF-LB produces. It is critical to understand what exactly is different between wrought and AM microstructures and why such differences exist to enable the development of solutions. Haynes 230 is typically used in high temperature structural applications for its microstructural stability and oxidation

resistance [1.7]. Creep, a time dependent form of permanent deformation that occurs at stresses below the quasistatic yield strength, is critical to understand before implementing AM products into high temperature structures. To enable the implementation of PBF-LB processed Haynes 230 for creep limited structures in gas turbine applications, the following two questions are proposed to guide research efforts:

- (1) How does the creep of a modified, highly printable version of Haynes 230 compare to both the unmodified alloy processed with PBF-LB and wrought material?

There are few data available in creep literature on the performance of PBF-LB Haynes 230, and it is not well understood how the alloy performs as an AM product rather than as a wrought product. It is hypothesized that creep rupture life of PBF-LB Haynes 230 could match that of wrought material if cracking could be eliminated. This is the basis for Chapter 3. Even with a foundational understanding of creep mechanisms for a given alloy, there is still a bottleneck in validating materials and processes for critical structural applications due to the time intensive nature of conventional creep testing. There is an unmet need for a method of acquiring large amounts of creep data within a timeline that aligns well with design windows, so engineers are often limited to using legacy processes and products, which prevents them from taking advantage of new alloys and processing routes. To help explore the possibility of high throughput creep testing to evaluate PBF-LB Haynes 230, the second question was proposed:

- (2) How well does stress relaxation testing of PBF-LB Haynes 230 predict conventional creep test results, and what are important considerations/limitations of the technique?

Stress relaxation testing has been studied for decades as a proxy for creep, but it has not been compared to conventional creep tests explicitly or used as a predictive method for creep rupture time. This is the basis for Chapter 4.

1.1 References

- [1.1] *Electric Power Monthly*. U.S. Energy Information Administration. June 2024.
- [1.2] P. Breeze. *Gas-Turbine Power Generation*, First Edition. Academic Press. 2016.
- [1.3] I. Gibson, D. Rosen, B. Stucker. *Additive Manufacturing Technologies*, 2nd Edition. Springer. 2015.
- [1.4] T. Raza, O. Adegoke, L. Squillaci, M. Neikter. Processing of high-performance materials by laser beam powder bed fusion. In: *Additive Manufacturing Materials and Technologies*. Elsevier. 123–154. 2024.
- [1.5] D. Gong, Q. An, R. Chen, S. Wang, L. Huang, L. Cui, W. Lu, L. Geng. Realizing Crack Inhibition of Haynes 230 Alloy during Laser Powder Bed Fusion by Grain Refinement under Decreased Energy Density. *Additive Manufacturing Frontiers*. Vol. 3, Iss. 3, 200139. 2024.
- [1.6] S. C. Ernst. Weldability Studies of Haynes 230 Alloy. *Welding Journal*, Vol. 73:4. 1994.
- [1.7] D. L. Klarstrom, H. M. Tawancy, D. E. Fluck, M. F. Rothman. A New Gas Turbine Combustor Alloy. *Proceedings of the ASME 1984 International Gas Turbine Conference and Exhibit, Volume 5: Manufacturing Materials and Metallurgy*, V005T11A003. 1984.

CHAPTER 2

BACKGROUND

2.1 Laser Beam Powder Bed Fusion

Laser beam powder bed fusion has become one of the foremost metal additive manufacturing technologies [2.1]. Boasting excellent spatial resolution, PBF-LB can create fine and complex features that would otherwise be difficult or impossible to manufacture with conventional methods like machining. PBF-LB is also efficient with feedstock as the only material consolidated is that which comprises the part, so excess metal powder can be used for additional prints. A wide range of industries have benefited from PBF-LB AM, including rapid prototyping, aerospace and power generation, and medical implants [2.2]. Currently, PBF-LB enables complex and one-off part designs with a variety of processible materials. Nevertheless, there are many alloys that are difficult to use with PBF-LB [2.3], but a wider range of applications could benefit if the processability with PBF-LB could be improved. Challenges can arise during powder production, AM processing, post-build heat treatment, and steps in between each. Naturally, this creates a need for manipulating existing materials to make them suitable for PBF-LB. Some modifications may come in the form of process parameter modification, such as optimizing temperatures and flow rates during gas atomization powder production, adjusting AM parameters, or refining heat treatment schedules. Other modifications consist of alloy modification, such as adding inoculant particles or modifying element concentrations to promote heterogeneous nucleation and grain refinement to eliminate solidification cracking. However, the influence of changes in composition and or microstructure to eliminate defects on relevant mechanical properties must be understood.

2.2 Creep

One of the major deformation modes for structural materials in high temperature applications with long service lives is creep. In these environments, alloys are subjected to stresses generally below their quasistatic yield strength for extended periods of time. At temperatures greater than about half of the alloy's melting point (T_m), diffusion and therefore dislocation climb take place more readily. Generally, dislocation climb and glide dominate deformation at temperatures nearer to $0.5 T_m$ and moderate stresses [2.4]. Diffusional creep takes

place at temperatures approaching T_m or at lower stresses that are insufficient to cause dislocations to move throughout the microstructure [2.4]. Diffusivities are higher at grain boundaries relative to within grains due to the free space between mismatched crystal lattices, so reducing grain boundary area perpendicular to the tensile direction is a method to reduce diffusional creep rates [2.4]. Accordingly, directionally solidified and single crystal parts have been implemented and are used for the most demanding and operationally critical components, such as early-stage turbine blades.

PBF-LB enables a different strategy for reducing the impact of creep for demanding structural applications. Complex part geometries can include cooling channels that reduce the effective operating temperature that a component experiences. For example, the ability to produce complex designs can enable new cooling technologies to be implemented that can drastically reduce metal temperatures [2.5]. Improved cooling technologies can enable higher engine operating temperatures which promotes greater efficiency. Paired with the ability to consolidate multiple parts assemblies into a single component, PBF-LB is a competitive option for new designs for cleaner and more efficient power generation and aerospace propulsion. To enable these potential benefits to be realized, the creep properties of materials processed with PBF-LB must be understood.

2.3 Stress Relaxation Testing

Conventional creep testing typically involves measuring strain as a function of time up to a preset amount of creep strain or to rupture at a constant engineering stress and temperature. While these methods have the highest fidelity to actual use cases, they are time intensive. A single creep test run at actual service stresses until sample failure can require 1000s – 100,000s of hours (months – decades) for just one result [2.6]. For a new alloy or new processing technique to be used for critical application where creep will take place, extensive validation testing must be completed, which can take decades. The bottleneck that creep testing poses can be reduced by implementing a testing technique that accelerates the collection of creep data. Stress relaxation testing is effectively a self-programmed, variable stress/strain rate creep test that can generate data corresponding to those from several hour to several thousand-hour conventional creep tests with a single experiment in less than 100 hours [2.7]. This plethora of data, combined with principles relating minimum creep rates and stresses to theoretical rupture times, allows for comparisons to be made between stress relaxation tests and conventional creep

tests. Up to now, stress relaxation testing has not been extensively applied to PBF-LB or been used to directly compare to conventional creep tests. Therefore, further work is needed to determine if stress relaxation testing can be used as a high throughput technique for creep property evaluation.

2.4 References

- [2.1] I. Gibson, D. Rosen, B. Stucker. Additive Manufacturing Technologies, Second Edition. Springer. 2015.
- [2.2] S. Kamara, K. S. Faggiani. Fundamentals of additive manufacturing for the practitioner, First Edition. John Wiley & Sons, Inc. 2021.
- [2.3] J. N. DuPont, J. C. Lippold, S. D. Kiser. Welding Metallurgy and Weldability of Nickel-Base Alloys. John Wiley & Sons, Inc. 2009.
- [2.4] M. E. Kassner. Fundamentals of Creep in Metals and Alloys. Elsevier. 2015.
- [2.5] C. K. Stimpson, J. C. Snyder, K. A. Thole, D. Mongillo. Effectiveness Measurements of Additively Manufactured Film Cooling Holes. Journal of Turbomachinery. Vol. 140, No. 1. 2018.
- [2.6] T. Tanski, M. Sroka, A. Zielinski. Creep. IntechOpen, 1, 19. 2018.
- [2.7] D. A. Woodford. Stress Relaxation Testing of Service Exposed IN738 for Creep Strength Evaluation. Journal of Engineering for Gas Turbines and Power. Vol. 122, 451–456. 2000.

CHAPTER 3

CREEP OF A STANDARD AND MODIFIED VERSION OF LASER POWDER BED FUSION-PROCESSED HAYNES 230

Modified from a manuscript in progress with a planned submission to MSE A.

Daniel McConville¹, Ben Rafferty², Kevin Eckes², Jeremy Iten², Amy Clarke¹, Jonah Klemm-Toole¹

3.1 Abstract

Haynes 230 is a solid solution and carbide precipitation strengthened nickel alloy often used in gas turbine engines. While the alloy is arc weldable, efforts to introduce the alloy to laser powder bed fusion additive manufacturing have been hindered by the presence of solidification cracking which severely debits mechanical properties. In this study, the creep performance of standard laser powder bed fusion processed Haynes 230 at 760 °C is compared to a modified, crack-free version of the alloy. The modified version of Haynes 230 exhibits lower minimum creep rates, higher creep ductilities, and longer rupture times compared to standard Haynes 230. Analysis using a creep rupture time model indicated that the primary factor leading to the longer creep life in the modified Haynes 230 is the lower minimum creep rate, although the finer grain size in the modified alloy also made a small contribution to the longer creep life. Due to the increases in creep performance, the modified version of the alloy shows similar creep behavior to wrought Haynes 230, while the standard version of the alloy shows considerably degraded creep performance. The results of this work show that minor compositional and microstructural modification is a meritorious pathway to manufacture legacy alloys with novel techniques such that the advantages which additive manufacturing offers, like increased component complexity and part consolidation, can be realized without developing new alloy systems.

¹ Colorado School of Mines, Metallurgical and Materials Engineering Department; 1500 Illinois St., Golden, CO 80401

² Elementum 3D; 400 Young Court, Erie CO 80516

3.2 Introduction

Haynes 230 is a nickel-based alloy developed for improved high temperature performance to replace more expensive alloys with elevated cobalt content [3.1]. The primary use case for Haynes 230 was originally considered to be gas turbine combustor hardware, so the alloy was designed to have excellent formability and weldability. Featuring a solid solution strengthened FCC γ matrix with additional carbide precipitate strengthening, Haynes 230 is designed to further precipitation harden while in service to offer substantial creep strength, particularly at low strains. M_6C carbides form during hot processing around 1177 °C to inhibit grain growth and $M_{23}C_6$ carbides precipitate at lower temperatures relevant to turbine operating conditions for improved creep performance [3.1–3.3]. These strengthening mechanisms provide good creep strength at temperatures exceeding those where γ' and γ'' strengthened alloys exhibit precipitate dissolution [3.3]. Manufacturing Haynes 230 with laser beam powder bed fusion (PBF-LB) additive manufacturing (AM) offers many benefits from design and performance standpoints. Complex part features like cooling channels enable gas turbines to operate with higher efficiencies. Furthermore, Haynes 230 is under consideration for use in advanced ultra-supercritical steam and nuclear applications, accelerating the transition to cleaner energy production [3.4, 3.5].

Despite its weldability in arc-based processes, Haynes 230 suffers from solidification cracking when manufactured with PBF-LB similar to many other Ni-based alloys [3.6, 3.7]. Solidification cracking can be reduced or eliminated by modifying either the thermal conditions during solidification or the composition to result in grain refinement. Adjusting laser parameters has been proven to be effective at eliminating cracking by Wu et al. [3.8]. Several other studies explore adding particles, including TiC, Y_2O_3 , and TiB₂, that provide greater heterogeneous nucleation site density [3.9–3.12]. One group added Zr to increase the amount of constitutional undercooling during solidification [3.13]. Others have utilized the synergistic effect of increasing both undercooling *and* nucleation site density to reduce grain size and texture, yielding crack-free material [3.14]. Even though cracking has been eliminated in a variety of ways in PBF-LB Haynes 230, very little high temperature mechanical property data, including creep, is available in the literature.

This study aims to provide a basic understanding of its creep performance and a rationalization of how the compositional and microstructural modifications needed to eliminate solidification cracking influence creep characteristics. Standard Haynes 230 containing

solidification cracking and a modified version that is crack-free were creep tested at 760 °C. The microstructures were analyzed before and after creep testing to understand how creep damage accumulates in each material. A creep rupture model was used to interpret how microstructure changes in the modified alloy contribute to improved creep performance compared to the standard version. By eliminating solidification cracking and drastically improving creep performance in a formerly unprintable material, this study demonstrates how legacy alloys can be modified to be compatible with novel manufacturing techniques for the next generation of high temperature structural applications.

3.3 Methods

3.3.1 Sample Processing

Standard Haynes 230 powder was supplied by Höganäs (product designated Ni230) and modified by Elementum 3D to improve laser powder bed printability (product designated Ni230 RAM1). The composition of the Ni230 powder is shown in Table 3.1. Ni230 RAM1 was modified with the addition of 0.29 wt% Ti and 0.11 wt% B₄C, each in powder form, and is referred to hereafter as the “modified” alloy. The Ti is intended to fully melt and provide additional constitutional undercooling while the B₄C are intended to remain solid and act as nucleation sites, employing the synergy between undercooling and inoculation described by others [3.14]. Samples were additively manufactured with an EOS M 290 PBF-LB machine using 1500 mm/s raster velocity, 300 W laser power, 40 μm layer height, and 70 μm hatch spacing. An example build plate containing horizontal (XY) bars, vertical (Z) bars, and cubes for metallographic analysis is shown in Figure 3.1. The horizontal bars were printed on a foot to reduce overhang, and the cylindrical portion for all bars measured 16 mm in diameter and 120 mm in length. The cubes measured 15 mm × 15 mm × 15 mm. Bars were removed from the build plate and solution heat treated at 1230 °C for 1 hour followed by air cooling prior to machining. Figure 3.1 shows a schematic of the tensile specimens used. The specimens were machined to a 0.4 μm Ra finish with no additional polishing.

Table 3.1. Composition of Ni230 as reported in the product specification.

Cr	W	Mo	Mn	Si	Al	C
21.40	13.70	1.90	0.68	0.48	0.38	0.07
Co	Fe	Ta	Ti	Nb	B	Ni
0.06	0.03	0.02	0.01	0.01	0.009	Bal.

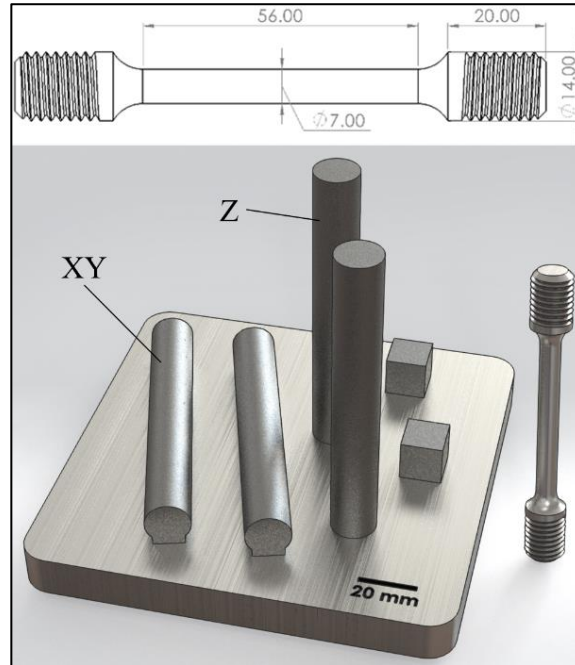


Figure 3.1. Illustration of horizontally and vertically oriented bars, metallography cubes, and a machined creep specimen. Machining dimensions in mm.

3.3.2 Creep Testing

Creep testing was performed in air on horizontal Ni230 (Ni230-XY), horizontal Ni230 RAM1 (Modified-XY) and vertical Ni230 RAM1 (Modified-Z) with a Zwick Roell Kappa 50 DS electromechanical load frame equipped with a clamshell furnace. Three engineering stresses were tested on one sample of each material/orientation: 145 MPa, 160 MPa, and 190 MPa. Stress was applied at an engineering strain rate of $8.3 \times 10^{-5} \text{ s}^{-1}$ and held constant for the full duration of each test until rupture. The test temperature of 760 °C, a value that is relevant to many gas turbine and other power generation applications, was controlled by two N-type thermocouples wired to the upper and lower portions of each sample's 56 mm parallel section, approximately 40 mm apart. A contact extensometer with a 50 mm gauge length was inserted into the furnace

approximately 2 cm away from the sample during heat up and attached when the temperature equilibrated. The maximum temperature fluctuation observed was 0.4 °C. The extensometer could only measure 25 mm of displacement, so it was removed prior to reaching 50 % strain. In tests with greater than 50 % strain, extensometer data is used to determine strain up to the point of removal, and the crosshead position is used to calculate strain from that point up to rupture. In all cases, extensometer measurements were used to determine the minimum creep rate which occurred within the first few percent of creep strain.

3.3.3 Microstructural Characterization

Prior to any creep testing, metallographic cubes in the as-built (AB) and solution heat treated (HT) condition were analyzed to assess general build quality, degree of solidification cracking, carbide characteristics, and grain size. Standard metallographic preparation consisted of sectioning cubes in the Z plane, grinding with 200 grit and 400 grit fixed abrasive, and polishing with 9 μm, 6 μm, 3 μm, and 1 μm diamond suspensions. This provided quality sufficient for optical microscopy on an Olympus DSX 500 digital optical microscope. Prior to general imaging with a TESCAN S8252G scanning electron microscope (SEM), a mixed acids etchant, comprised of equal parts concentrated acetic, hydrochloric, and nitric acids, was swabbed on each sample for 10-20 seconds to reveal grain boundaries and carbides. Electron backscatter diffraction (EBSD) analysis on an FEI Helios Nanolab 600i SEM was performed after an additional vibratory polishing step with 0.05 μm colloidal silica for 18-24 hours. All SEM imaging was done with an accelerating voltage of 20 kV and 15 mm working distance. For EBSD grain size measurements, three fields of view at 200 × magnification were captured for each sample and analyzed with OIM software. Image analysis for carbide area fraction measurements was performed manually on high contrast SEM micrographs with the particle analysis package in ImageJ software.

Following creep testing, SEM imaging and EBSD were again employed to analyze fracture surfaces, post-test microstructure, and creep deformation. The build direction is difficult to ascertain in the XY-built samples since it is only known to be perpendicular to the tensile direction.

3.3.4 Creep Data Analysis

Creep curves contain strain as a function of time where test time and creep strain are set to zero at the point which the engineering stress setpoint is reached. Ni230 undergoes almost no “steady state” creep [3.17] but rather switches nearly immediately from primary creep to tertiary creep, so the inflection point is identified as the instant at which minimum creep rate takes place. To ascertain the minimum creep rate, a polynomial fit is applied to the strain versus time curve about the data near the inflection point such that the coefficient of determination is greater than 0.999. The derivative of the equation of fit is taken and the local minimum is found, yielding the minimum creep rate for a given test. Minimum creep rates are plotted on a Norton diagram of minimum creep rate versus stress. A general creep model shown in Equation 3.1 was fit to the data where $\dot{\epsilon}_{min}$ is the minimum creep rate; A is a constant that depends on temperature, σ is the applied stress; and n is the stress exponent [3.16].

$$\dot{\epsilon}_{min} = A\sigma^n \quad (3.1)$$

Fitting the model to the data in the Norton diagram allowed for the determination of the stress exponent, which is useful for interpreting dominant creep mechanisms where a value between 5 and 10 corresponds to power law creep for Ni alloys. [3.18]. Finally, the Larson-Miller parameter is employed to compare creep rupture times between tests completed in this study and those found in literature [3.19].

To interpret the differences in creep performance between standard and modified Ni230, a creep rupture time model that considers void growth on an isolated grain boundary facet perpendicular to an applied tensile stress was explored [3.15]. Considerable experimental data is needed to predict creep rupture time using the model. Instead, we utilize the model to understand how aspects that vary between the standard and modified versions of Ni230 contribute to the observed differences in rupture time. As creep damage develops and culminates in rupture, the creep voids can be considered to instantaneously nucleate or continuously nucleate at grain boundaries during creep. Additionally, creep voids can be assumed to grow purely through diffusion without any constraint of the surrounding grains, or the growth rate of the voids can be assumed to be constrained by the rate at which the surrounding grain can creep. It has been found that the model considering continuous nucleation and constrained growth to predict time to void coalescence best matches experimental creep rupture times in steels and Ni-based alloys, and this form is shown in Equation 3.2 [3.15]:

$$t_c = 0.38 \left[\frac{\pi(1 + 3/n)}{\dot{N}} \right]^{1/3} \frac{\omega_f}{(\dot{\epsilon}g)^{2/3}} \quad (3.2)$$

where t_c is the time to void coalescence; n is the creep stress exponent; ω_f is the critical void area fraction at grain boundaries (assumed to be $\pi/4$ consistent with [3.15]); $\dot{\epsilon}$ is the macroscopic minimum creep rate; and g is grain size. The creep void nucleation rate, \dot{N} , is a function of the minimum creep rate and therefore stress (through Eq. 1), shown in Equation 3.3:

$$\dot{N} = \alpha' \dot{\epsilon} = \alpha' A \sigma^n \quad (3.3)$$

where α' is proportionality constant that describes how fast voids nucleate during creep deformation, and A and n have the same meaning as in Eq. 3.1. Differences in grain size, minimum creep rate, and the rate at which voids nucleate during creep between standard and modified Ni230 can be used to estimate the effects of each quantity on rupture time.

Experimentally measured grain sizes and minimum creep rates for both materials are used, but because void nucleation during was not experimentally assessed, the α' term was fit to the creep results of standard and modified Ni230 to estimate changes in void nucleation during creep between the two materials.

3.4 Results

3.4.1 Microstructure Prior to Creep Testing

Figure 3.2 shows optical micrographs of standard (A) and modified (B) Ni230 in the as-built condition. Significant solidification cracking is observed in standard Ni230 but is completely eliminated in modified Ni230, which is attributed to the grain refinement enabled by compositional modification. In EBSD inverse pole figure + image quality (IPF+IQ) maps of as-built standard (C) and modified (D) Ni230, it is evident that solidification cracks tend to occur at regions of high misorientation, such as grain boundaries. Figure 3.2 also contains SEM SE micrographs of each respective alloy (E and F) in the solution heat treated condition, where it can be seen that the modified version of Ni230 contains a considerably higher fraction of carbides. Table 3.2 summarizes the as-built alloy density and area average EBSD grain size along with the intragranular carbide area fractions observed in the solution heat treated condition. It is evident that the as-built densities of the standard and modified materials are not significantly different, but there are substantial differences between the grain size and intragranular carbide area fraction.

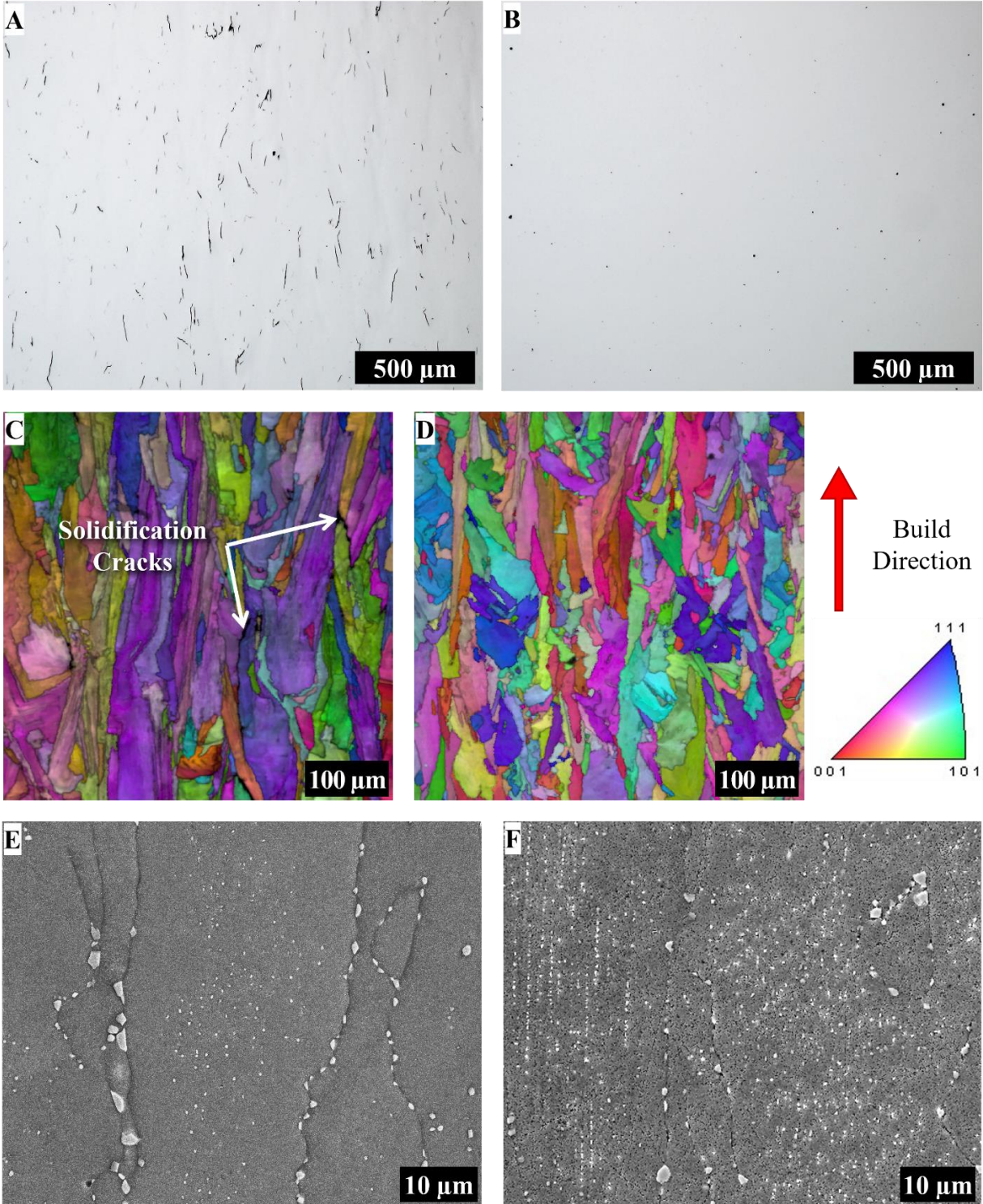


Figure 3.2. Optical micrographs of as-built A) standard and B) modified Ni230. EBSD IPF + IQ maps of C) standard and D) modified Ni230, also in the as-built condition. SEM SE micrographs of mixed acids etched E) standard and F) modified Ni230 in the solution heat treated condition. Orientations in the IPF + IQ maps are with respect to the build direction.

Table 3.2. Microstructure characteristics of standard and modified PBF-LB Haynes 230 in the as-built (AB) and solution heat treated (HT) conditions.

Parameter	Standard Ni230	Modified Ni230
Relative Density (AB) [%]	99.37	99.93
EBSD Grain Size (AB) [μm]	85.0 ± 8	41.0 ± 8
Carbide Area Percentage (HT) [%]	0.67	2.44

3.4.2 Creep Results

Figure 3.3 shows the results of creep testing at 145, 160, and 190 MPa at 760 °C for the material conditions evaluated. The standard Ni230 samples exhibited the shortest rupture time and lowest creep ductility at each stress compared to the modified version of the alloy. The Z-oriented samples of the modified alloy consistently showed slightly lower rupture times compared to the XY-oriented samples. Creep ductility of the XY-oriented sample from the modified alloy is slightly lower than the Z-oriented sample at 190 MPa, but larger creep ductility is observed in the XY-oriented samples at 160 and 145 MPa samples. In general, both orientations of the modified alloy showed much improved creep performance compared to the standard form of Ni230.

Minimum creep rate as a function of engineering stress for each alloy and condition are shown in Figure 3.4. For a given stress, the modified Ni230 samples show lower minimum creep rates compared to standard Ni230 samples. Furthermore, the XY-oriented samples of modified Haynes 230 show lower minimum creep rates than the Z-oriented ones, which is atypical and discussed in section 3.5.3. The stress exponents, ranging from 5.9 to 7.5, are consistent with dislocation glide and climb, or power law creep, being the dominant creep mechanism. Furthermore, this range of stress exponents contains the value for wrought Haynes 230 at 760 °C, reported to be 6.3 [3.3]. In general, the conditions that show lower minimum creep rates also show longer rupture times, which is discussed in context of the rupture time model in section 3.5.1. A summary of values pertaining to the creep tests, including time to 1% creep strain, are shown in Table 3.3.

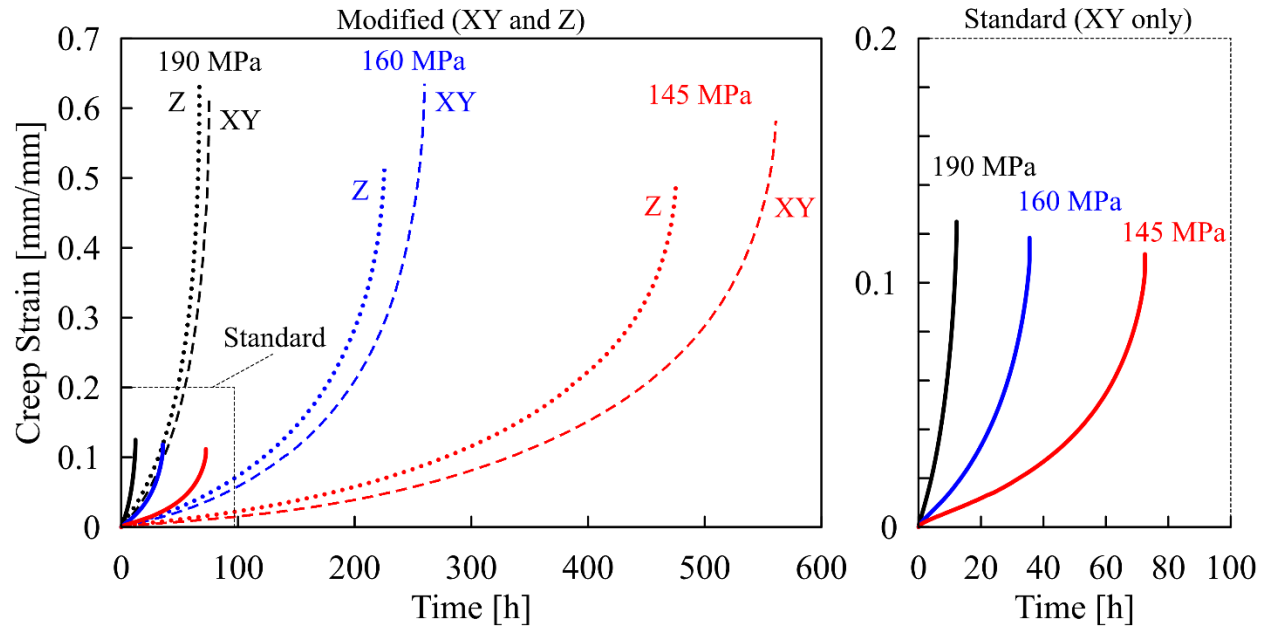


Figure 3.3. Creep strain vs. time curves of each alloy at 145, 160, and 190 MPa stresses. Region of interest highlights the tests on standard Haynes 230, which consisted of only XY samples.

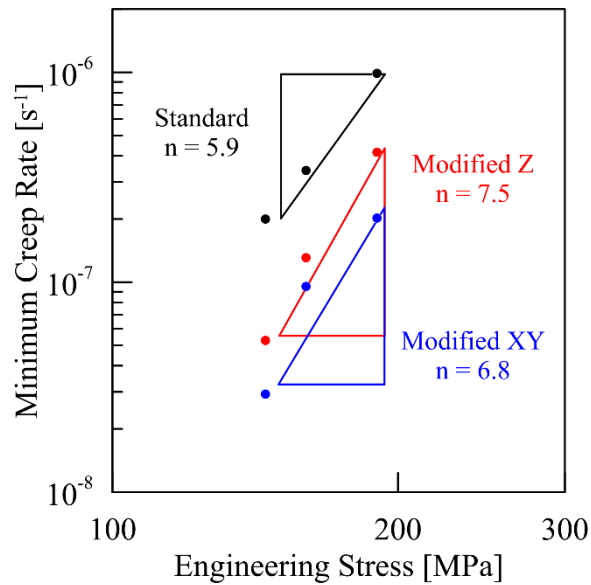


Figure 3.4. Minimum creep rate vs. stress (Norton plot) indicating the creep stress exponent obtained from the three tests on each.

Table 3.3. Summary of creep data.

Parameter	Stress [MPa]	Standard XY	Modified XY	Modified Z
Time to 1% [h]	145	16.78	62.76	45.47
	160	7.66	24.98	18.92
	190	2.15	2.48	2.36
Rupture Time [h]	145	72.52	560.93	475.61
	160	36.17	259.94	225.58
	190	12.19	76.8	67.03
Min. Creep Rate [s ⁻¹]	145	2.00E-7	2.92E-8	5.27E-8
	160	3.41E-7	9.53E-8	1.31E-7
	190	9.88E-7	2.02E-7	4.15E-7
Creep Strain at Rupture [%]	145	11.2	58.3	49.4
	160	11.8	63.5	51.3
	190	12.5	61.5	63.5

To compare the results of the creep tests performed here to tests at different temperatures and stresses in the literature, the Larson-Miller parameter is used. Figure 3.5 shows stress versus Larson-Miller parameter of the samples tested in this study, a region encompassing the reported performance of Haynes 230 in wrought form (the lower bound of which is comprised of sheet data and the upper bound of plate data) [3.20], and data from a study which reportedly eliminated solidification cracking in PBF-LB Haynes 230 through parameter adjustments [3.8]. The creep performance of the modified alloy (both XY and Z oriented) falls well within the range of wrought material, approaching that of plate in the case of the XY-oriented samples. Clearly, the standard Haynes 230 condition performs far below that of wrought or the modified alloy from this work. It is curious that even though solidification cracking was minimized in the data from Wu *et al.*, the creep performance appears to be equally worse than wrought when compared to standard Ni230 that has extensive solidification cracking in the present study. This result is an indication that the lower creep performance of standard Ni230 may not entirely be a result of microcracking, but that there are other microstructural contributors.

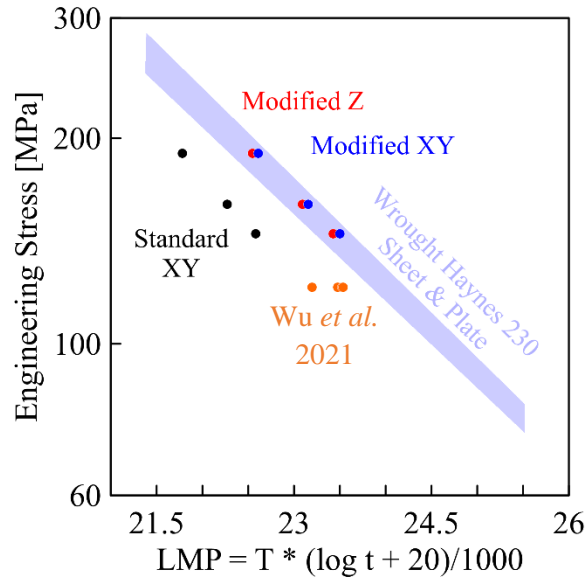


Figure 3.5. Stress vs. Larson-Miller parameter comparing standard and modified PBF-LB Ni230 from this work to wrought Haynes 230 [3.20] and PBF-LB Haynes 230 from Wu *et al.* 2021 [3.8].

3.4.3 Deformation and Fracture of Creep Specimens

Figure 3.6 is a side-by-side comparison of standard XY, modified Z, and modified XY Ni230 creep samples tested at 145 MPa to illustrate the drastic differences in the degree to which each material necked prior to fracture. The standard specimen shows no noticeable necking and primary fracture perpendicular to the tensile axis with no noticeable shear lips. In comparison, the samples of the modified alloy show noticeable non-uniform deformation and shear lips, which correspond to the much larger creep ductility shown in Figure 3.3. By analyzing the fracture surfaces, shown in Figure 3.7, it is clear that the standard and modified versions of Haynes 230 exhibit different fracture mechanisms. Standard Ni230 shows a considerable portion of smooth fracture features that may be solidification cracks present prior to testing combined with some microvoids between the smooth features. The modified alloy, in both orientations, exhibits microvoids throughout the fracture surface. In summary, the modified Haynes 230 samples showed much greater deformation (including necking) prior to fracture and exclusively microvoids on the fracture surface whereas the standard Haynes 230 sample exhibited no noticeable necking and a large portion of smooth featureless fracture which is likely related to pre-existing solidification cracks.



Figure 3.6. Comparison of deformation in 145 MPa creep samples of standard Haynes 230 (XY-oriented), modified Haynes 230 (XY-oriented), and modified Haynes 230 (Z-oriented).

3.4.4 Microstructure After Creep Testing

The gauge sections near the fracture surface of failed creep samples were sectioned and characterized to evaluate microstructure evolution and creep damage. Figure 3.8 shows EBSD IPF maps of standard Ni230 (XY-oriented), modified Ni230 (XY-oriented), and modified Ni230 (Z-oriented) after creep testing at 145 MPa. Cracking primarily at grain boundaries with very little obvious intragranular deformation is seen in the standard Ni230 sample. The intergranular cracking is likely a combination of pre-existing solidification cracking and coalesced creep voids that formed at grain boundaries. Conversely, the modified alloy shows isolated creep voids distributed throughout the microstructure and what appears to be extensive deformation, elongation, and potentially some dynamic recrystallization of the grains along the tensile axis indicated by the distinct, reoriented grains at primary boundaries. Each EBSD map is paired with etched SEM SE micrographs to highlight the degree to which intragranular carbides continued to precipitate during testing. The area fraction of intragranular carbides in standard Ni230 increased moderately from 0.67 % to 0.87 % while modified Ni230 rose from 2.4 % to 4.3 %. The much larger increase in the area fraction of intragranular carbides, which is evident in both orientations of the modified alloy, likely contributes to its lower minimum creep rate (higher creep strength).

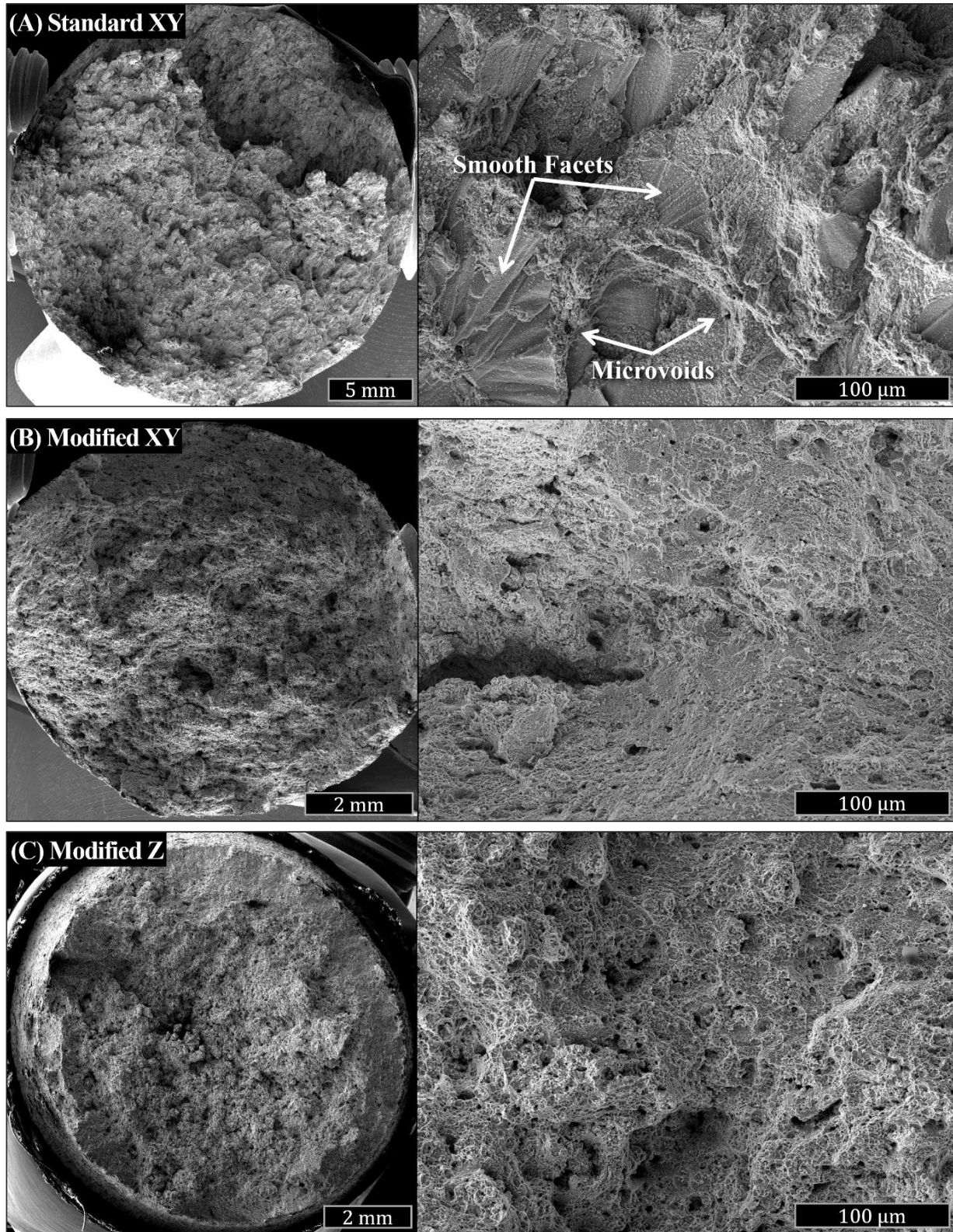


Figure 3.7. SEM SE micrographs of fracture surfaces of A) standard XY-oriented, B) modified XY-oriented, and C) modified Z-oriented Ni230 from 145 MPa creep tests.

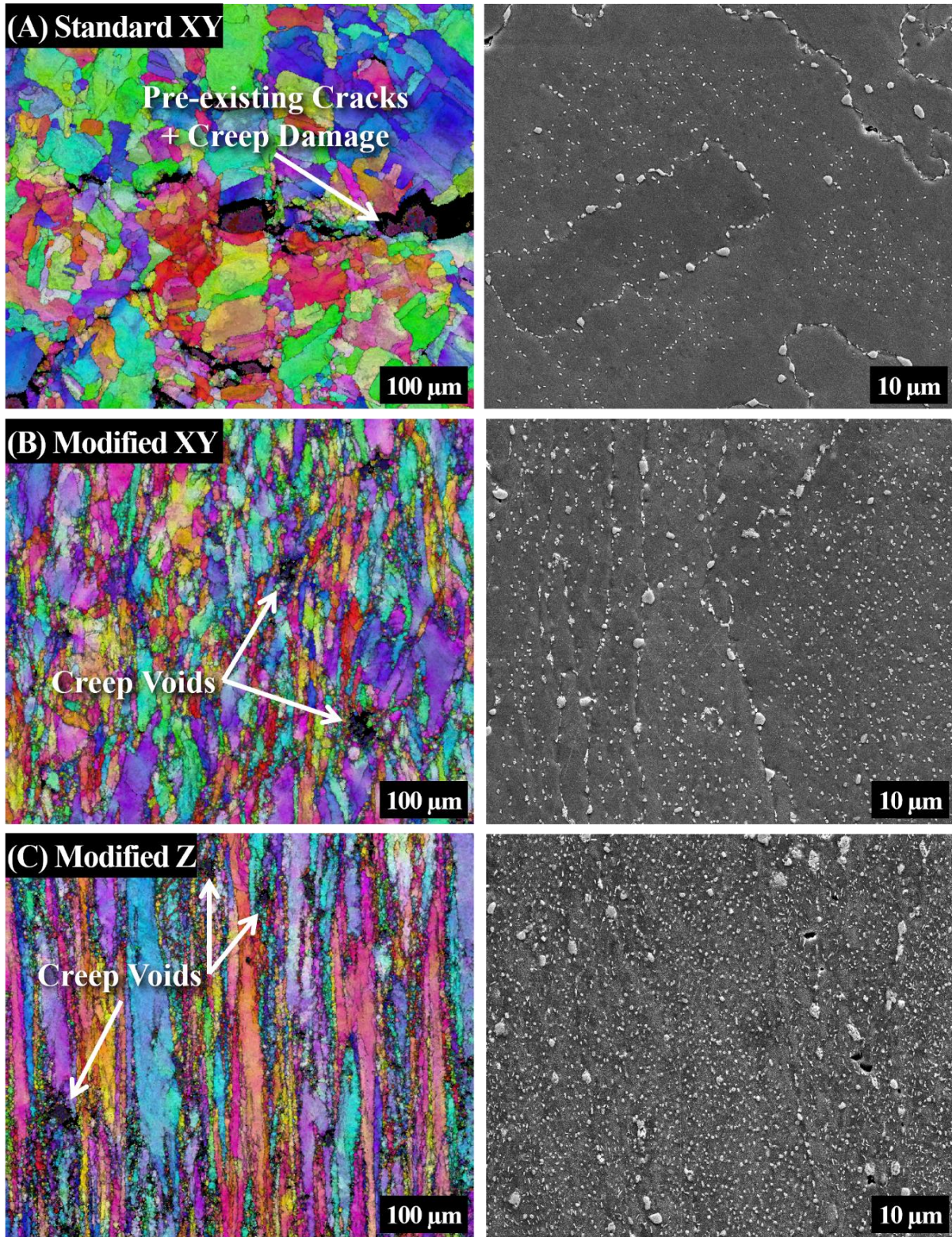


Figure 3.8. EBSD IPF maps of A) standard XY, B) modified XY, and C) modified Z Ni230 just below fracture surfaces from 145 MPa tests illustrating significant differences in creep deformation. IPF coloration is oriented to the vertical direction, which corresponds to the tensile direction of the creep samples. Accompanying SEM SE micrographs illustrate carbides.

3.5 Discussion

3.5.1 Contributions to Improved Creep Performance in Modified Ni230

Figure 3.9 contains plots of rupture time as a function of stress with points for each XY-oriented creep test result and lines representing predictions from the creep rupture model with the goal of illustrating how different microstructure features in the modified version of the alloy result in improvements in creep rupture time over the standard alloy. The blue lines for Figures 3.9A and 9B use the same values in the model as for standard Ni230 except that Figure 3.9A uses the minimum creep rate terms (A and n) from the modified alloy and Figure 3.9B uses the grain size (g) from the modified alloy. This enables an estimation of the influence that the grain refinement and lower minimum creep rate of the modified alloy have on improved creep rupture life when compared to the standard alloy. To assess the contribution of the proportionality constant α' , which describes the rate of void nucleation during creep straining, to variations in rupture time, the solid blue line shows model predictions with all numerical values for the modified alloy except the value of α' that best fits the data for the standard alloy. The dashed blue line shows the same model predictions for the modified alloy but uses the value of α' that best fits the data for the modified alloy.

By inspection of Figure 3.9, it is clear that the lower minimum creep rate in the modified version of the alloy makes the largest contribution to the longer rupture time compared to standard Ni230. The reduction in grain size that contributed to solidification crack elimination in the modified alloy makes a much smaller contribution to the increased rupture time. Grain size has an effect on the minimum creep rate as well, which cannot be decoupled from the creep void nucleation term, but evaluating it individually suggests that most of the creep strengthening comes from another source. The degree to which α' must be changed to align properly with experimental data was found to be negligible, indicating that both materials nucleate creep voids at approximately the same rate as a function of creep rate.

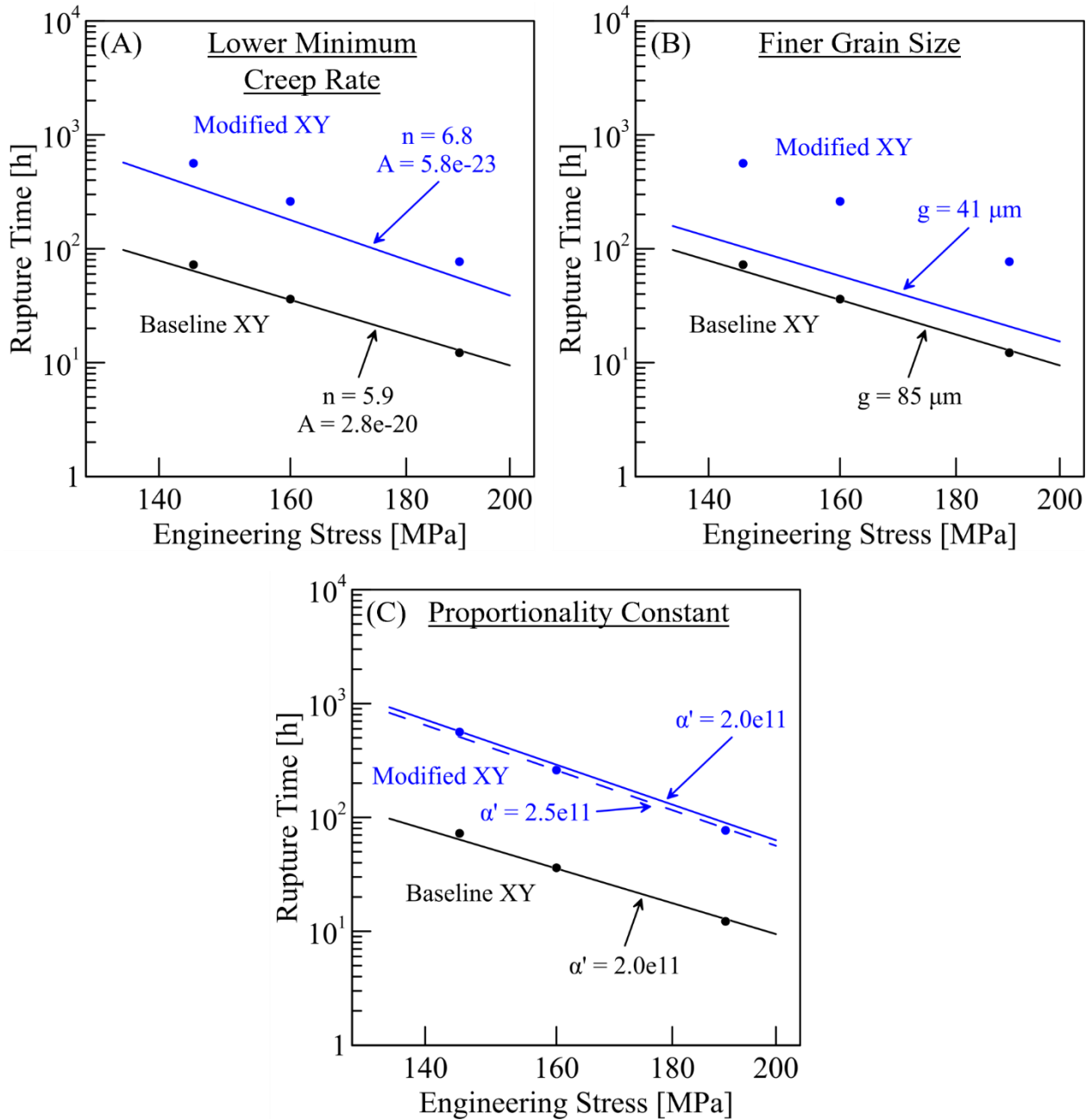


Figure 3.9. Plots of rupture time vs. stress comparing the influence of A) minimum creep rate B) grain size on the rupture time of standard and modified Ni230. Figure 3.9C shows the influence that the rate at which voids nucleate during creep strain (proportionality constant, α') has on model fit to experimental data.

While the assessment here is adequate to explain the creep improvements in the modified alloy, a more sophisticated model (or combination of models) that account for pre-existing cracks, creep ductility, and fracture mechanism may provide additional insight and may have predictive potential. Creep ductility is likely affected by the presence of pre-existing

microcracks, but the model used here does not explicitly predict it. Dynamic recrystallization has been noted as the primary softening mechanism in wrought Haynes 230 [3.22] and is observed to a degree in failed creep samples of modified Ni230 (Figure 3.8). Dynamic recrystallization eliminates certain grain boundaries, which could prevent void growth and require additional nucleation at new boundaries, further increasing the time to coalescence and rupture. Some models that were explored by Riedel and others, as discussed by Kassner, account for cracks already present [3.16]. It would be worthwhile to investigate these models, but they rely heavily on geometric factors that can be difficult to garner from microstructures. In short, additional models are needed to better understand how the pre-existing cracks in standard Ni230 contribute to lower creep ductility and ultimately poor creep performance.

3.5.2 Contribution of Microstructural Features to Improved Creep Strength in the Modified Alloy

Prior to creep testing, the modified Ni230 had a 1.7 % greater intragranular carbide area fraction than the standard alloy. This amount would be substantial enough to promote higher creep strength (lower minimum creep rate) on its own, but the additional intragranular precipitation that takes place during creep further improves modified Ni230 (4.3 %) over standard (2.4 %). The degree of carbides precipitation is, of course, influenced by the time held at temperature. The low rupture time of standard Ni230 may detract from its ability to precipitate the maximum amount of carbides. Grain size typically has minor effects on the minimum creep rate in power law creep, although finer grain sizes have been reported to result in lower minimum creep rates [3.16]. It is possible that the finer grain size in the modified alloy also contributes to lower minimum creep rates, but this effect is likely much smaller compared to the higher fraction of intragranular carbides. Conversely, a finer grain size could promote creep void nucleation due to the greater availability of grain triple points and overall grain boundary area, so when competing against grain size strengthening, the net creep strengthening effect may be dulled.

It is worth noting that the highly refined as-solidified microstructure afforded by PBF-LB enables carbides to be very finely and uniformly dispersed within grains. The same does not appear to be the case in wrought forms where it is evident that large carbides reside at grain boundaries and intragranular carbides tend to be too large to provide considerable strengthening [3.2, 3.3, 3.21]. The improved carbide dispersion and greater precipitation strengthening may be

largely responsible for enabling modified Ni230 to match the creep performance of wrought Haynes 230.

3.5.3 Atypical Creep Anisotropy

It is generally expected that additively manufactured Ni-based alloys will exhibit pronounced creep anisotropy, due to strong crystallographic texture and elongated grain morphologies [3.23-3.26]. Typically in these cases, minimum creep rates are lower and rupture times are longer when tested in vertical (Z) orientations where elongated grains effectively reduce the grain boundary area relative to a horizontal (XY) orientation. The same was not observed in this study as minimum creep rates of the XY-oriented samples are consistently lower (and rupture times longer) than the Z-oriented samples for modified Ni230. Given the ability of the modified Ni230 to elongate substantially during high temperature testing, this phenomenon may be explained by the relative ease for grain boundary sliding to occur in vertical samples. The increase in grain boundary sliding in the vertical samples may contribute to the higher minimum creep rates relative to horizontal samples and could contribute to the lower rupture time. It would be expected that the converse would be true in diffusional creep for which lower grain boundary area aligned with the tensile direction would result in lower minimum creep rates and accordingly longer rupture times.

3.5.4 Influence of Crack Elimination on Creep Life

When compared by Larson-Miller parameter, the XY-oriented modified Ni230 outperforms PBF-LB Haynes 230 that is reportedly free of solidification cracks [3.8]. In fact, the standard Ni230 in this work performs equally poor relative to wrought Haynes 230 compared to the work by Wu *et al.* [3.8]. This finding suggests that simply eliminating cracking is insufficient to allow PBF-LB Ni230 to exhibit creep resistance similar to wrought Haynes 230. The Ti and B₄C additions to modified Ni230 induce grain refinement and, more importantly, provide additional carbide precipitation that increase creep strength such that its rupture time reflects the range expected for wrought Haynes 230. This key result can help guide efforts to design new Ni-based alloys specifically for PBF-LB in creep limited applications.

3.6 Conclusions

Laser powder bed fusion processed samples of Ni230 that contain solidification cracking and a modified version of Ni230 without cracking were creep tested at 760 °C. Characterization before and after creep testing was performed to quantify differences in microstructural features between standard and modified Ni230 that lead to differences in creep performance. A creep rupture model was employed to interpret what factors lead to the improved creep performance of the modified alloy. Based on the results of this work, the following conclusions are made:

- The modified Haynes 230 showed longer rupture times and higher creep ductility than the standard alloy when creep tested with constant engineering stresses of 145 MPa, 160 MPa, and 190 MPa at 760 °C. Horizontal (XY-oriented) samples of the modified alloy showed longer rupture times compared to vertical (Z-oriented samples).
- The modified Haynes 230 alloy showed lower minimum creep rates (higher creep strength) than standard Haynes 230, although both materials appear to be deforming in power law creep within the conditions evaluated. XY-oriented specimens exhibited lower minimum creep rates than Z-oriented specimens
- The higher creep strength in the modified Haynes 230 alloy is likely due to a greater fraction of intergranular carbides prior to creep testing and a greater amount of dynamic precipitation during creep testing.
- The fracture surface of standard Haynes 230 shows a large fraction of smooth features that are interpreted to be pre-existing solidification cracks in addition to some creep voids at grain boundaries. In contrast, the modified alloy shows exclusively voids that are distributed throughout the highly deformed microstructure which likely accounts for the higher creep ductility.
- The results of a creep rupture time model suggest that the lower minimum creep rate in the modified alloy is the primary contributor to longer rupture times compared to standard Haynes 230. The finer grain size also contributes to the longer rupture time, but to a much lesser degree.
- Overall, the creep performance of the modified PBF-LB Haynes 230 is equivalent to wrought Haynes 230, and the results of this work show that existing Ni-based alloys can be tailored to improve additive manufacturability and performance for high temperature structural applications.

3.7 Acknowledgments

This material is based upon work supported by the Office of Naval Research under contract No. N68335-22-C-0443. Any opinions, findings and conclusions or recommendations expressed in this material are those of the author(s) and do not necessarily reflect the views of the Office of Naval Research. Equipment used in this study was funded through the National Science Foundation (DMR-1828454).

Author contributions to this work are as follows: *Daniel McConville*: Investigation, Methodology, Formal Analysis, Data Curation, Visualization, Writing – Original Draft, Writing – Review & Editing. *Ben Rafferty*: Resources, Funding Acquisition, Writing – Review & Editing. *Kevin Eckes*: Funding Acquisition, Project Administration, Writing – Review & Editing. *Stan Baldwin*: Resources, Writing – Review & Editing. *Jeremy Iten*: Funding Acquisition, Project Administration, Writing – Review & Editing. *Amy Clarke*: Funding Acquisition, Writing – Review & Editing. *Jonah Klemm-Toole*: Conceptualization, Methodology, Funding Acquisition, Supervision, Writing – Review & Editing.

3.8 References

- [3.1] D. L. Klarstrom, H. M. Tawancy, D. E. Fluck, M. F. Rothman. A New Gas Turbine Combustor Alloy. Proceedings of the ASME 1984 International Gas Turbine Conference and Exhibit, Volume 5: Manufacturing Materials and Metallurgy, V005T11A003. 1984.
- [3.2] S. C. Ernst. Weldability Studies of Haynes 230 Alloy. *Welding Journal*, Vol. 73:4. 1994.
- [3.3] C. J. Boehlert and S. C. Longanbach. A comparison of the microstructure and creep behavior of cold rolled HAYNES® 230 alloyTM and HAYNES® 282 alloyTM. *Materials Science and Engineering A*, 528, 4888–4898. 2011.
- [3.4] F. Abe. Research and Development of Heat-Resistant Materials for Advanced USC Power Plants with Steam Temperatures of 700 °C and Above. *Engineering*, Vol. 1, Iss. 2, 211–224. 2015.
- [3.5] M. Katcher, D. L. Klarstrom. A Review of Haynes 230 and 617 Alloys for High Temperature Gas Cooled Reactors. ASME 2007 Pressure Vessels and Piping Conference, Vol. 6, 425–430. 2007.
- [3.6] Y. Wang, W. Guo, H. Zheng, Y. Xie, X. Zhang, H. Li, M. Xu, H. Zhang. Microstructure, crack formation and improvement on Nickel-based superalloy fabricated by powder bed fusion. *Journal of Alloys and Compounds*, Vol. 962, 171151. 2023.
- [3.7] J. N. DuPont, J. C. Lippold, S. D. Kiser. *Welding Metallurgy and Weldability of Nickel-Base Alloys*. John Wiley & Sons, Inc. 2009.

- [3.8] Wu, S. R. Yarasi, J. Seo, N. Lamprinakos, A. D. Rollett. Study of the Printability, Microstructures, and Mechanical Performances of Laser Powder Bed Fusion Built Haynes 230. *Metals*, 12, 1380. 2022.
- [3.9] Y. Zhao, J. He, B. Li, Z. Gao, Q. Guo, Z. Ma, Y. Liu. The role of ceramic particles on the crack inhibition and mechanical properties improvement of Haynes 230 alloy fabricated by laser powder bed fusion. *Journal of Materials Processing Technology*, 320, 118124. 2023.
- [3.10] Q. Han, Y. Gu, J. Huang, L. Wang, K. W. Q. Low, Q. Feng, Y. Yin, R. Setchi. Selective laser melting of Hastelloy X nanocomposite: Effects of TiC reinforcement on crack elimination and strength improvement. *Composites Part B: Engineering*, 202, 108442. 2020.
- [3.11] Z. Zhang, Q. Han, S. Yang, Y. Yin, J. Gao, R. Setchi. Laser powder bed fusion of advanced submicrometer TiB₂ reinforced high-performance Ni-based composite. *Materials Science and Engineering A*, 817, 141416. 2021.
- [3.12] Z. Zhang, Q. Han, Z. Liu, X. Wang, L. Wang, X. Yang, T. Ma, Z. Gao. Influence of the TiB₂ content on the processability, microstructure and high-temperature tensile performance of a Ni-based superalloy by laser powder bed fusion. *Journal of Alloys and Compounds*, 908, 164656. 2022.
- [3.13] Y. Zhao, Z. Ma, L. Yu, Y. Liu. New alloy design approach to inhibiting hot cracking in laser additive manufactured nickel-based superalloys. *Acta Materialia*, 247, 118736. 2023
- [3.14] Y. Zhao, T. Ma, Z. Gao, Y. Feng, C. Li, Q. Guo, Z. Ma, Y. Liu, Significant reduction of grain size and texture intensity in laser powder bed fusion fabricated nickel-based superalloy by increasing constitutional supercooling. *Composites Part B: Engineering*, 266, 111040. 2023.
- [3.15] H. Riedel. *Fracture at High Temperatures*. 1987.
- [3.16] M. E. Kassner. *Fundamentals of Creep in Metals and Alloys*. Elsevier. 233–260. 2015.
- [3.17] G. J. Pataky, H. Sehitoglu, H. J. Maier. Creep deformation and mechanisms in Haynes 230 at 800 °C and 900 °C. *Journal of Nuclear Materials*, Vol. 443, Iss. 1–3, 484–490. 2013.
- [3.18] M. E. Kassner. Five-Power-Law Creep. In: *Fundamentals of Creep in Metals and Alloys*. Elsevier. 233–260. 2015.
- [3.19] F. R. Larson, J. Miller. *Transactions ASME*. 74, 765–771. 1952.
- [3.20] Haynes 230 Brochure. Haynes International, 2021. www.haynesintl.com/wp-content/uploads/2023/06/230-brochure.pdf.
- [3.21] R. Luo, Q. Liu, P. Gao, T. Liu, H. Ding, D. Zhang, Y. Cao, X. Cheng. Effect of microstructural evolution and mechanical properties of Haynes 230 superalloy during long-term aging at 700°C. *Journal of Alloys and Compounds*, Vol. 947, 169495. 2023.
- [3.22] Y. Liu, R. Hu, J. Li, H. Kou, H. Li, H. Chang, H. Fu. Deformation characteristics of as-received Haynes230 nickel base superalloy. *Materials Science and Engineering A*, Vol. 497, Iss. 1–2, 283–289. 2008.

- [3.23] S. Megahed, K. M. Krämer, C. Heinze, C. Kontermann, A. Udoh, S. Weihe, M. Oechsner. Influence of build orientation on the creep behavior of IN738LC manufactured with laser powder bed fusion. *Materials Science and Engineering A*, 878, 145197. 2023.
- [3.24] K. Kianinejad et al. Creep anisotropy of additively manufactured Inconel-738LC: Combined experiments and microstructure-based modeling. *Materials Science and Engineering A*, 907, 146690. 2024.
- [3.25] J. J. Shi et al. Microstructure and creep anisotropy of Inconel 718 alloy processed by selective laser melting. *Materials Science and Engineering A*, 805, 140583. 2020.
- [3.26] A. D. Shaikh, F. Schulz, K. Minet-Lallemand, E. Hryha. Microstructure and mechanical properties of Haynes 282 superalloy produced by laser powder bed fusion. *Materials Today Communications*, Vol. 26, 102038. 2021.

CHAPTER 4

STRESS RELAXATION TESTING AS A HIGH THROUGHPUT METHOD FOR ASSESSING CREEP STRENGTH IN LASER POWDER BED FUSION PROCESSED NI-BASED SUPERALLOYS

Derived from a paper pending publication in proceedings of the Superalloys 2024 conference.

© Copyright 2024 The Minerals, Metals & Materials Society. Used with permission.

Daniel McConville¹, Ben Rafferty², Kevin Eckes², Jeremy Iten², Amy Clarke¹, Jonah Klemm-Toole¹

4.1 Abstract

Ni-based superalloys processed by laser beam powder bed fusion (PBF-LB) additive manufacturing (AM) are ideal for high temperature structural applications in the aerospace and power generation industries due to the increased component complexity afforded by AM. However, conventional creep testing limits the rate at which new materials can be produced with AM. To help accelerate the acceptance of AM Ni-based alloys for high temperature applications, methods for high-throughput creep evaluation are needed. The stress relaxation test has potential to hasten the development and validation of PBF-LB Ni-based structural alloys by assessing a wide range of creep rates relevant to service conditions with a single test. In this work, alloy Ni230, a gas atomized powder derivative of Haynes 230, and variant thereof containing added TiC are assessed. Each material was subjected to a limited subset of conventional creep tests accompanied by stress relaxation tests. Following the calculation methodology described herein, stress relaxation tests predict creep rates and rupture times that align well with conventional creep test results. Stress relaxation tests also reveal features of microstructural characteristics and evolution which are not readily apparent with other experiments. Several advantages and challenges with stress relaxation testing are discussed.

¹ Colorado School of Mines, Metallurgical and Materials Engineering Department; 1500 Illinois St., Golden, CO 80401

² Elementum 3D; 400 Young Court, Erie, CO 80516

4.2 Literature Review and Introduction

4.2.1 Characteristics of PBF-LB Haynes 230

Haynes 230 is a solid solution and carbide precipitation strengthened Ni-based alloy designed for high temperature structural applications such as gas turbine engines [4.1]. Its excellent formability and weldability in wrought form make it suitable for sheet metal components of gas turbine engines such as combustion cans, fuel swirlers, and other combustor hardware [4.2]. The highly complex designs of gas turbine combustor hardware make these components ideal for the application of additive manufacturing (AM); however, the high temperature mechanical properties, especially creep, of AM Haynes 230 are largely unknown.

Additive manufacturing processes such as laser powder bed fusion (PBF-LB) allow for unique features like in-wall cooling passages to be integrated without the need for multiple complex parts and extensive or impossible machining. Unfortunately, Haynes 230 experiences significant solidification cracking when manufactured by PBF-LB. Some studies report that cracking can be eliminated through process parameter optimization [4.3], while others suggest that adding inoculant particles [4.4–4.8] or modifying composition [4.9] can mitigate the issue. In the solution annealed state, wrought Haynes 230 typically contains large dispersed M_6C carbides. At service temperatures below 1150 °C, $M_{23}C_6$ forms and results in dynamic precipitation, improving creep strength during service [4.2]. In the case of PBF-LB Haynes 230, carbides are often present at interdendritic regions in the as-built condition, and these coarsen while others form at grain boundaries after solution annealing [4.3, 4.10]. There is very little work in the literature evaluating dynamic precipitation of carbides during elevated temperature mechanical loading of PBF-LB Haynes 230.

4.2.2 Motivation for Accelerated Testing

Alloys designed for use in gas turbine applications are generally intended to be in service for months to decades [4.11]. Creep rupture testing these materials on such a timeline is unfeasible, so instead, short term test data are extrapolated to identify stresses that result in acceptably low creep rates such as 0.01 % per 1000 hours [4.12]. Acquiring these values still requires hundreds of hours of testing. Of course, there are many wrought and cast alloys which have been in service for decades and do not require further creep study [4.13]. New alloys or existing alloys processed with new manufacturing technologies such as AM, though, typically

require extensive testing, especially given the evidence that AM materials exhibit different mechanical performance compared to their cast and wrought counterparts [4.3, 4.10, 4.14, 4.15]. With the scale of the additive manufacturing industry today and the bottleneck posed by creep testing, there remains a need for a higher throughput method of assessing or predicting creep strength, rates, and rupture life.

4.2.3 Previous Applications of Stress Relaxation Tests

Stress relaxation testing is capable of predicting creep rates over a wide range of stresses with a single test, which has the potential to provide information on creep strength in a high throughput manner. Early work on developing an understanding of creep and stress relaxation tests was done mainly on aluminum, presumably for the ease of testing and availability of creep data [4.16]. Realizing the capability of stress relaxation testing to evaluate creep properties, researchers began applying the method to steels and nickel alloys [4.17, 4.18]. Efforts to use stress relaxation tests to predict rupture have been mentioned, but attempts have only been made to estimate the time to reach certain creep strains [4.19]. It is more common for stress relaxation tests to accompany conventional creep tests for comparing minimum and average creep rates [4.20]. Recent studies have evaluated stress relaxation creep properties on AM materials [4.21, 4.22], but they have not been used widely to evaluate creep strength of additively manufactured alloys.

A more rapid acquisition of accurate creep data can enable faster validation of new and existing alloys, especially those which are used in PBF-LB and other additive manufacturing processes. Bottlenecked in part by creep testing, progress toward increased engine efficiency can occur sooner with a higher throughput creep assessment methodology. So long as an application-relevant microstructure is tested, stress relaxation has the potential to provide an understanding of creep behavior significantly quicker than traditional creep testing methods allow, offering the opportunity to rapidly test new and existing AM alloys and enabling quicker qualification for their use in creep-prone applications.

4.2.4 Objective of This Work

The objective of this work is to explore the use of stress relaxation testing as a high throughput tool to evaluate the creep properties of PBF-LB processed Haynes 230. Baseline PBF-LB Haynes 230 containing microcracks as well as a modified version of the alloy free of

microcracks were subjected to stress relaxation testing to determine minimum creep rates as a function of stress at 760 °C. Conventional creep tests were also conducted at 760 °C to provide a basis for comparison. A Monkman-Grant relationship was developed for both materials based on conventional creep testing results to enable rupture life predictions from the minimum creep rates obtained from stress relaxation testing. The results of this work are expected to shed light on the potential of stress relaxation testing to provide the high throughput creep property assessment capability needed to accelerate the development and validation of high temperature materials for structural applications.

4.3 Methodology

4.3.1 PBF-LB Processing

PBF-LB samples were processed on an EOS M 290 with 300 W laser power, 1500 mm/s raster velocity, 70 μm hatch spacing, and 40 μm layer height, resulting in an energy density of 71.4 J/mm³. The composition of Haynes 230 powder (referred to as Ni230 hereafter) is shown in Table 4.1. Solidification cracking was eliminated with grain refinement promoted by uniformly dispersing 0.25 wt% TiC with an average diameter of 0.4 μm in Ni230 powder (Ni230 TiC). Cubes with dimensions of 15 mm × 15 mm × 15 mm were evaluated for cracking analysis and build quality. Samples for conventional creep tests and stress relaxation tests were cylinders measuring 16 mm in diameter and 120 mm in length. They were built upon a rectangular foot to avoid excessive overhang and manufactured in the XY orientation, or parallel to the build plate as shown in Figure 1. Creep testing in the XY orientation ensures that the tensile stress is perpendicular to the solidification crack plane, maximizing the influence on mechanical properties in microcracked Ni230.

Table 4.1. Composition of Haynes 230 (Ni230) powder used for specimen manufacturing. All values in wt% reported by the powder manufacturer.

Cr	W	Mo	Mn	Si	Al	C
21.40	13.70	1.90	0.68	0.48	0.38	0.07
Co	Fe	Ta	Ti	Nb	B	Ni
0.06	0.03	0.02	0.01	0.01	0.009	Bal.

The PBF-LB bars were removed from their build plate before being solution heat-treated at 1230 °C for 2 hours, followed by forced air cooling. Round creep specimens were machined

with M14 threads and a 56 mm by 7 mm diameter parallel length, resulting in a 108 mm overall length as shown in Figure 4.1. Each specimen was machined to a $0.4 \mu\text{m Ra}$ finish but no additional polishing was performed.

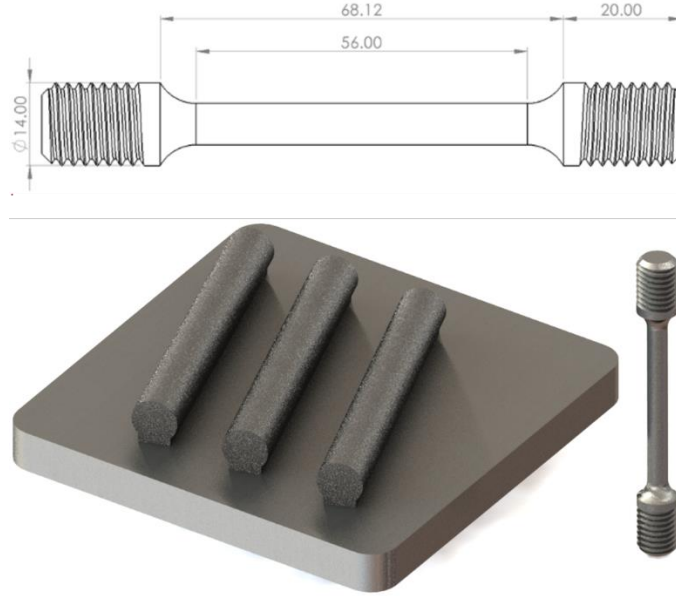


Figure 4.1. Schematic diagram of the PBF-LB samples on a build plate and the mechanical test specimens.

4.3.2 Mechanical Testing

A stress relaxation test evaluates the creep strength of the microstructure that is present during the test. For this test to accurately replicate the minimum creep rate of a conventional creep test, the microstructure (dislocation density and arrangement, precipitate distribution, etc.) at the minimum creep rate of the conventional creep test must also be present in the stress relaxation test specimen. For simplicity, it was initially assumed that applying the plastic strain at the minimum creep rate found in a conventional creep test to the sample at the beginning of a stress relaxation test will result in the same microstructural state, as suggested by Woodford [4.23]. Accordingly, a limited subset of conventional creep tests were conducted to identify the plastic strain (ϵ_p) at the minimum creep rate over a range of stresses at $760 \text{ }^\circ\text{C}$. The test temperature of $760 \text{ }^\circ\text{C}$ was selected because it is relevant to a wide range of power generation applications and creep data on wrought forms of Haynes 230 is available at this temperature as well. With these parameters, stress relaxation tests can be established with a range of total mechanical strains (ϵ_m^t) at the beginning of the tests, replicating the range of plastic strains experienced at the minimum creep rate of conventional creep tests. The lower bound of the total

strain at the beginning of the stress relaxation tests consists of the strain up to the yield point, which is comprised of elastic strain (ε_e) and zero macroscopic plastic strain (ε_p), as shown in Equation 4.1. The upper bound of the total mechanical strain at the beginning of the stress relaxation tests consists of the sum of ε_e and the greatest ε_p at the point of minimum creep rate identified in the conventional creep tests, as indicated in Equation 4.2.

$$\text{Lower bound: } \varepsilon_m^t = \varepsilon_e \quad (4.1)$$

$$\text{Upper bound: } \varepsilon_m^t = \varepsilon_e + \varepsilon_p \quad (4.2)$$

To extract the creep rate as a function of stress from a stress relaxation test, Equation 4.3 is employed, where $\dot{\varepsilon}_p$ is the plastic strain rate (or minimum creep rate), E is the elastic modulus, and $\frac{d\sigma}{dt}$ is the slope of the stress vs. time curve collected throughout the stress relaxation test. The elastic modulus (or more specifically, specimen stiffness) is estimated from the initial loading portion of the stress relaxation test and $\frac{d\sigma}{dt}$ can be evaluated by directly calculating the slope of the stress vs. time curve or applying a mathematical expression to the curve and computing the derivative.

$$\dot{\varepsilon}_p = -\frac{1}{E} \frac{d\sigma}{dt} \quad (4.3)$$

Stress relaxation tests as applied here only estimate the minimum creep rate as a function of stress at the temperature of the test. In order to predict rupture time (t_r), the Monkman-Grant (M-G) relationship was utilized, which asserts that the product of the minimum creep rate (raised to a constant β) and rupture time is a constant (α) for a given material condition, as shown in Equation 4.4 [4.24, 4.25]. These constants can be evaluated by fitting a power expression to conventional creep test data with minimum creep rate as a function of rupture time.

$$\dot{\varepsilon}^\beta t_r = \alpha \quad (4.4)$$

To facilitate the comparison of creep performance of the PBF-LB Ni230 and Ni230 TiC to wrought Haynes 230 evaluated at different temperatures (T) and stresses, the Larson-Miller parameter (LMP) is used, shown in Equation 4.5 [4.26].

$$LMP = T(\log t_r + 20) \quad (4.5)$$

To establish the strains to be applied for stress relaxation testing and identify the M-G constants to calculate creep rate as in Equation 4.3, three conventional creep tests to rupture were

performed at 190 MPa, 160 MPa, and 145 MPa on both alloys. All conventional creep tests and stress relaxation tests were performed on a ZwickRoell Kappa 50 DS electromechanical creep testing frame with a clamshell furnace and two N-type sample thermocouples. A 50 mm gauge length contact extensometer was used for the entire duration of each conventional creep test up to rupture and to hold each stress relaxation test at the desired strain. This strategy prevents compliance in the load string detracting from the accuracy of the set strain on the sample in accordance with ASTM E 328 [4.27]. In all cases, an engineering strain rate of $8.3 \times 10^{-5} \text{ s}^{-1}$ was used during the initial loading portion of conventional creep tests and stress relaxation tests. All tests were performed at a temperature setpoint 760 °C, and the maximum variation in temperature during the tests was less than 0.4 °C.

4.3.3 Microstructural Characterization

Metallographic preparation for optical microscopy (OM) consisted of grinding samples with 200 grit and 400 grit fixed abrasive diamond discs then polishing with 9 μm , 6 μm , 3 μm , and 1 μm diamond suspensions. An Olympus DSX 500 digital optical microscope was used to capture micrographs in the as-built sample condition to assess microcracking and general build quality. Samples for scanning electron microscopy (SEM) were prepared with the same polishing procedure with the added step of mixed acids etching, which consists of swabbing each sample with a solution of equal parts concentrated acetic, hydrochloric, and nitric acids for 10-20 seconds. SEM observation took place on a JEOL 7000F field emission scanning electron microscope using an accelerating voltage of 20 kV at a working distance of 15 mm in secondary electron imaging (SEI) mode. To measure intragranular carbide fractions, high contrast SEM micrographs were converted to binary images and selected areas were processed through particle analysis in ImageJ software. Finally, electron backscatter diffraction (EBSD) was completed on samples which received an additional 24-hour vibratory polishing step in 0.05 μm colloidal silica immediately following 1 μm diamond polishing. An FEI Helios Nanolab 600i scanning electron microscope equipped with an EDAX EBSD camera was used to collect diffraction patterns at $200 \times$ magnification and with an accelerating voltage of 20 kV. Inverse pole figure and image quality (IPF + IQ) micrographs were processed with neighbor pattern averaging and reindexing, neighbor confidence index correlation, and grain dilation cleanup in OIM software. Three fields of view were obtained using EBSD on each sample to estimate grain size.

4.4 Results

4.4.1 Microstructure in the As-built and Solution Heat Treated Conditions

Optical micrographs of Ni230 and Ni230 TiC are shown in Figure 4.2A and B, respectively, highlighting the complete elimination of microcracking with the addition of TiC. EBSD IPF + IQ maps of Ni230 and Ni230 TiC in the as-built condition are shown in Figure 4.2C and D highlighting grain refinement in Ni230 TiC that results in the elimination of microcracking. The average grain size of Ni230 is $91 \pm 8 \mu\text{m}$ whereas the average grain size of Ni230 TiC is $73 \pm 8 \mu\text{m}$. Negligible changes in grain size were observed after solution annealing. Figure 4.2E and F show etched micrographs of the same alloys after solution annealing. Carbides are observed at grain boundaries as well as former interdendritic regions within grains in both alloys. Ni230 TiC shows a significantly greater number of carbides dispersed within the grains compared to Ni230.

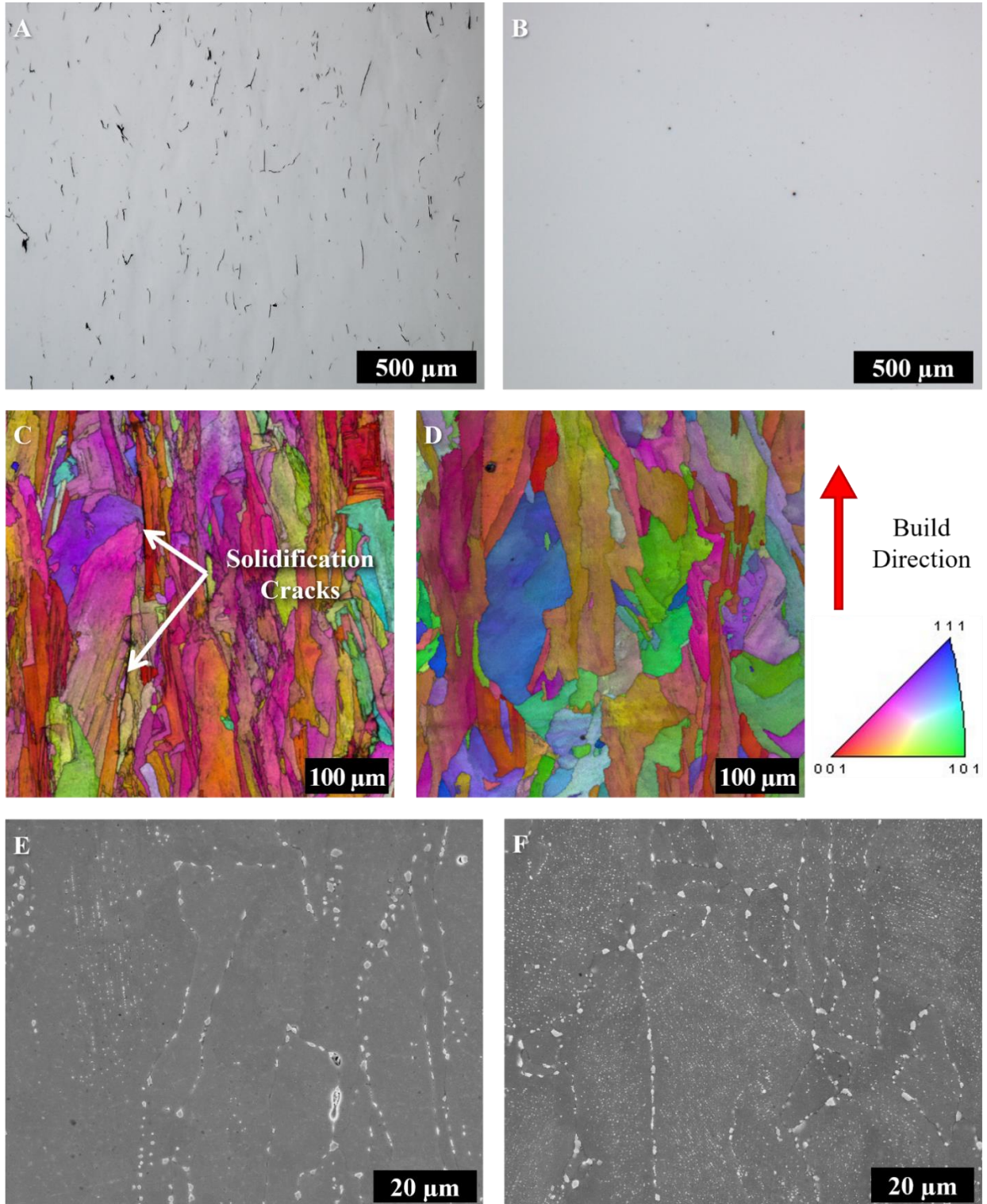


Figure 4.2. Light optical micrographs of A) Ni230 and B) Ni230 TiC in the as-built condition. EBSD IPF + IQ maps of C) Ni230 and D) Ni230 TiC in the as-built condition. The build direction and the IPF key is shown on the right of the figures. SEM SE micrographs of E) Ni230 and F) Ni230 TiC in the solution heat treated condition.

4.4.2 Stress Relaxation Testing

Table 4.2 contains the stress and respective rupture time of all conventional creep tests done on Ni230 and Ni230 TiC along with the plastic strain at the minimum creep rate used to establish stress relaxation test strain setpoints. For Ni230 and Ni230 TiC, the plastic strain at minimum creep rate from the 145 MPa tests were used to determine the strain setpoint for its high ϵ_p stress relaxation test.

Table 4.2. Creep data from conventional creep tests used for stress relaxation tests.

Alloy	Stress [MPa]	Rupture Time [h]	ϵ_p at Minimum Creep Rate [%]
Ni230	190	12.2	0.34
	160	36.2	0.65
	145	72.5	0.35
Ni230 TiC	190	50.9	0.57
	160	208.6	0.92
	145	455.8	1.54

Figure 4.3A shows the data of stress as a function of time collected for high plastic strain and zero plastic strain conditions for Ni230 and Ni230 TiC. Samples of each material were loaded to a strain just below their yield point and these tests are indicated as 0 % ϵ_p , or zero plastic strain at load application. Samples of each material were also subjected to a high ϵ_p representative of the plastic strains at the minimum creep rate from their respective conventional creep tests. In general, stresses relax quicker in the high plastic strain samples compared to the 0 % plastic strain samples. Ni230 TiC samples relax slower at higher stresses compared to Ni230 samples, but the Ni230 TiC samples continue to relax at lower stresses whereas the Ni230 samples appear to approach a stress plateau at lower stresses.

Perturbations in stress as a function of time which occur over 1 to 10 hours can be seen in all of the curves. The variation in strain during the tests was less than 1×10^{-4} , which indicates fluctuations induced by the mechanical test controller are not the cause but are instead evidence of microstructural evolution, a finding consistent with other studies that will be expanded upon in a later section [4.28–4.30]. To eliminate the complicating effects of the perturbations, the data were fitted with 4th order polynomials to stress as a function of $\ln(\text{time})$ to calculate smoothed

relaxation curves, illustrated in Figure 4.3B. The coefficients of determination (R^2) for all fits were greater than 0.98. Creep rates as a function of stress were then calculated from these fits in accordance with Equation 4.3.

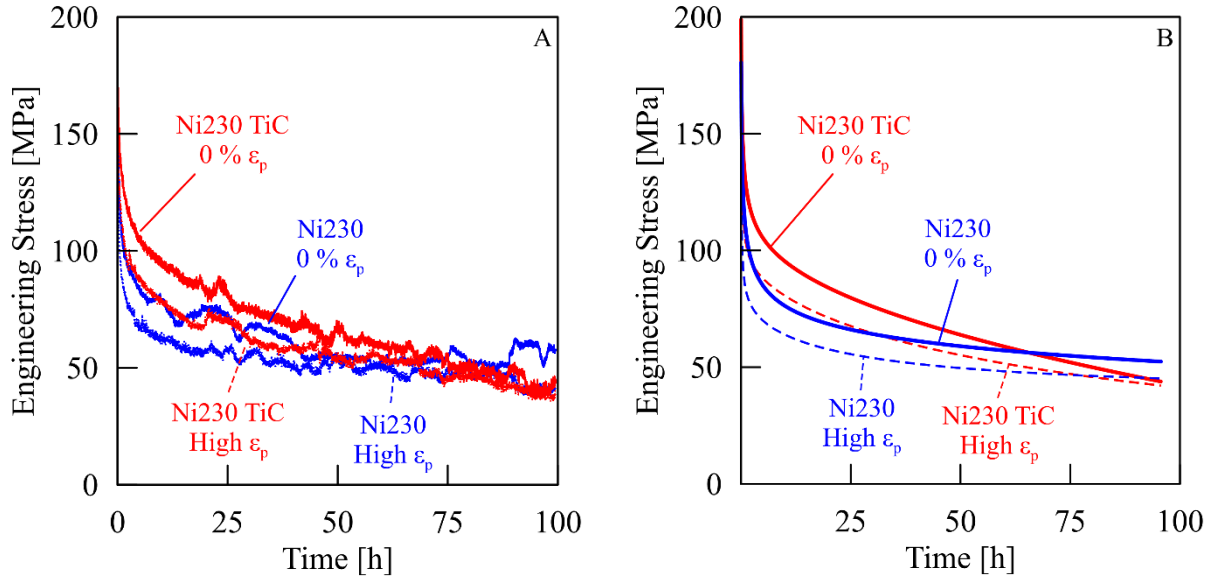


Figure 4.3. A) Stress as a function of time for both alloys and two strain conditions each. B) Smoothed stress relaxation curves

Figure 4.4 shows the calculated creep rate as a function of stress from each stress relaxation test performed as well as the minimum creep rate as a function of stress for each conventional creep test. It can be seen that, for both materials, the 0 % plastic strain stress relaxation tests show creep rates that more closely match minimum creep rates from conventional creep tests compared to the high plastic strain stress relaxation tests. An approximate stress exponent is indicated on the 0 % plastic strain stress relaxation curves and for the conventional creep tests to facilitate comparison. The stress exponents from stress relaxation tests and conventional creep tests are in closer alignment with Ni230 compared to Ni230 TiC. In general, the creep rates from stress relaxation tests are higher compared to minimum creep rates from conventional creep tests for both materials. Most notably, there is a transition of the stress exponent from 6.8 to 1.1 at lower stresses in Ni230 TiC, suggesting a transition in creep mechanism from power law to diffusional creep [4.25]. The transition to diffusional creep at a higher stress in Ni230 TiC relative to Ni230 may be due to the finer grain size of the Ni230 TiC condition with more grain boundary area available for diffusion to take place.

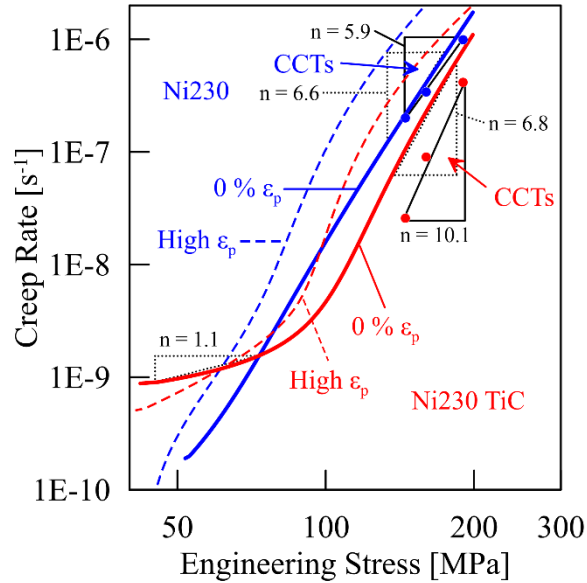


Figure 4.4. Creep rate as a function of stress for stress relaxation tests (SRTs) and conventional creep tests (CCTs).

Figure 4.5 shows the minimum creep rate versus rupture time for each conventional creep test completed on Ni230 and Ni230 TiC. The three points for each materials' conventional creep test were fit with power functions, which are used to calculate the parameters of the Monkman-Grant rupture relation shown in Equation 4.4. These Monkman-Grant relationships enable the estimation of rupture times from creep rate as a function of stress from stress relaxation tests.

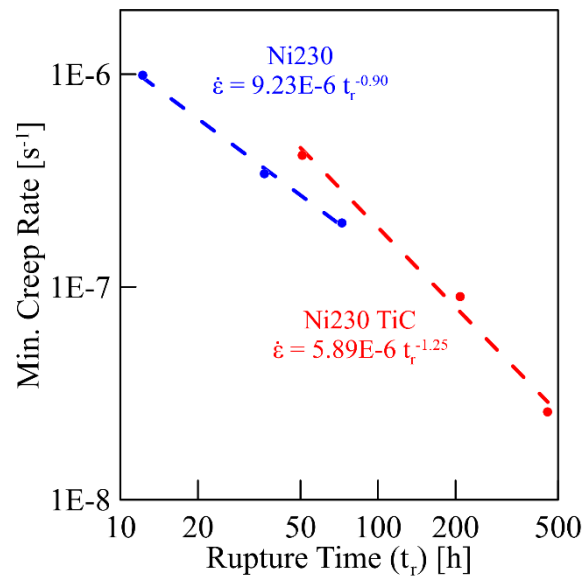


Figure 4.5. Minimum creep rate vs. rupture time of Ni230 and Ni230 TiC from conventional creep tests.

Finally, Figure 4.6 shows stress as a function of Larson-Miller parameter for rupture time containing each conventional creep test and the 0 % plastic strain stress relaxation tests for Ni230 and Ni230 TiC for stresses where power law creep is the dominant mechanism. A region encompassing the performance of wrought Haynes 230 in plate and sheet forms is indicated [4.1]. Owing to the better prediction of creep rate as a function of stress with the 0 % ϵ_p stress relaxation tests, only their predicted rupture times are included. Because the stress relaxation tests generally showed higher minimum creep rates than conventional creep tests, the rupture predictions from stress relaxation tests are slightly lower than the conventional creep test rupture times. It is noteworthy that the rupture times measured from conventional creep tests for Ni230 are considerably lower than those of sheet and plate wrought Haynes 230 likely due to the presence of microcracking. However, the creep rupture performance of Ni230 TiC falls within the range of wrought Haynes 230. Clearly, stress relaxation tests combined with the Monkman-Grant relation are capable of discerning the difference in creep performance between Ni230 and Ni230 TiC.

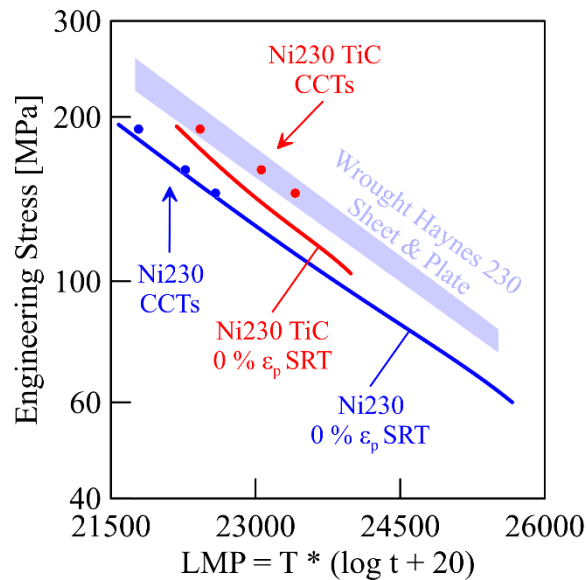


Figure 4.6. Stress versus Larson Miller Parameter (LMP) for conventional creep tests, 0 % plastic strain stress relaxation tests, and reported Haynes 230 data.

4.4.3 Microstructure Evolution During Stress Relaxation Testing

Figure 4.7 shows SEM SE micrographs of Ni230 and Ni230 TiC in the heat-treated condition and after 100-hour high plastic strain stress relaxation tests. As mentioned previously, the fraction of grain boundary carbides and carbides within the grains in Ni230 TiC is

significantly higher than in Ni230. Image analysis in the as-heat treated condition showed that the area fraction of intragranular carbides was determined to be 0.23 % in Ni230 and 0.67 % in Ni230 TiC. Both Ni230 and Ni230 TiC show noticeable increases in the fraction of carbides in the microstructure after the stress relaxation test indicating dynamic changes to the microstructure during thermal exposure. After 100 hours of exposure to 760 °C, the carbide area fractions in Ni230 and Ni230 TiC increased to 2.25 % and 6.14 %, respectively. These changes in microstructure during testing indicate that care must be taken to ensure that the microstructure experiencing the stress relaxation test is the one that is of interest for a given application.

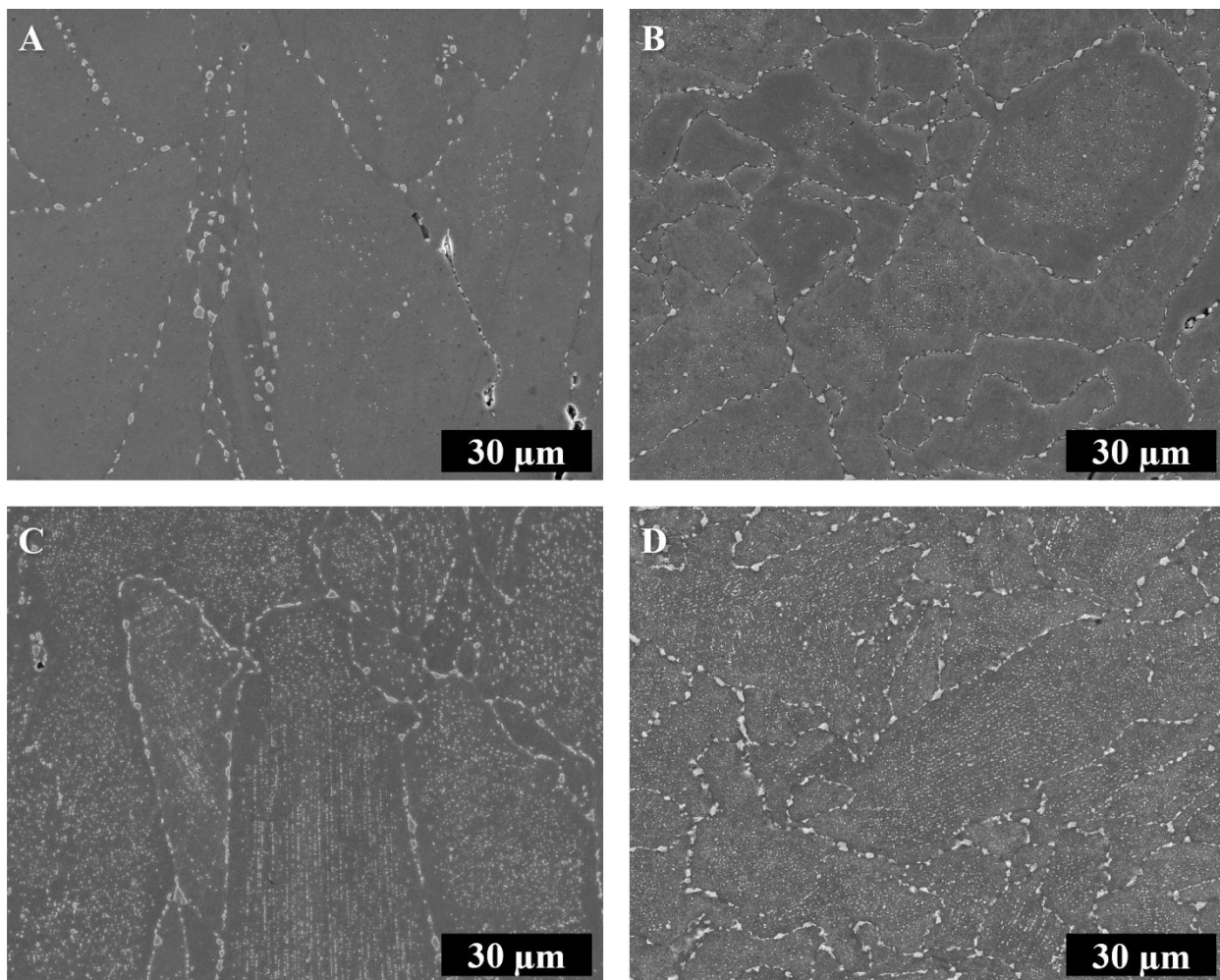


Figure 4.7 SEM SE micrographs of A) heat treated Ni230, B) Ni230 post-SRT, C) Heat treated Ni230 TiC, and D) Ni230 TiC post-SRT.

4.5 Discussion

4.5.1 Influence of Starting Strain Upon Loading on Stress Relaxation Tests

In the stress and temperature regime tested here, dislocation climb and glide is the primary mechanism by which creep occurs, indicated by the stress exponents ranging from 5.9-10 shown in Figure 4 [4.25]. A stress relaxation test is highly sensitive to the microstructure present during the test, so the mobile dislocation density at the start of a stress relaxation test will influence the observed creep rates. The original assumption made here following Woodford was that the microstructure of the stress relaxation test specimen would be most similar to that in the conventional creep tests when the plastic strain at the minimum creep rate from the conventional creep test was applied to the stress relaxation test [4.23]. This high plastic strain condition was found to drastically overestimate the creep rate as a function of stress compared to conventional creep tests as shown in Figure 4.4, therefore underestimating rupture life. The zero plastic strain tests predict rupture life considerably more accurately, coming within 3 % of the actual rupture life for Ni230 at 145 MPa.

The observation that the 0 % plastic strain stress relaxation test better matches conventional creep test results counters the original assumption that the plastic strain at the start of the stress relaxation test should be the plastic strain at the minimum creep rate of conventional creep tests. While the accumulated plastic strain may match between these testing methods, it is unlikely that the mobile dislocation densities and arrangements are similar between these conditions. As identified in a simple dislocation-based model for creep shown in Equation 4.6A–C, the creep rate is proportional to the mobile dislocation density [4.31]:

$$\dot{\epsilon} = \rho_m b \bar{v} \quad (4.6A)$$

$$\bar{v} = \left(\frac{\tau}{\tau_0} \right)^n \quad (4.6B)$$

$$\dot{\epsilon} = \rho_m b \left(\frac{\tau}{\tau_0} \right)^n \quad (4.6C)$$

where $\dot{\epsilon}$ is strain (or creep) rate; ρ_m is mobile dislocation density; b is the magnitude of the Burgers vector; \bar{v} is the average dislocation velocity; τ is the resolved shear stress; τ_0 is the resolved shear stress for unit velocity; and n is the stress exponent.

Stress relaxation tests with large amounts of plastic strain upon loading likely begin with higher mobile dislocation density since the plastic strain is applied in a fraction of the time that it takes for the minimum creep rate to be reached in the conventional creep tests. The longer time

to reach minimum creep rate in conventional creep tests allows for considerable recovery to occur that is not possible to the same extent in stress relaxation tests. Lower applied strains result in lower mobile dislocation densities at the beginning of the test and more accurately emulate the microstructure during conventional creep tests in this case. This finding is consistent with other studies where higher creep rates were observed for higher starting strain conditions [4.21, 4.32]. It has been reported that the dislocation density of Ni230 is very low following post-build heat treatment [4.33], so the dislocation density at the minimum creep rate in the conventional creep tests must be higher than in the heat-treated condition but still lower than when a significant amount of plastic strain is applied for a stress relaxation test. The dislocation density is lowest when the total strain applied upon initial loading does not exceed the yield point, which could be evaluated with hardness testing before stress relaxation.

4.5.2 Stress Relaxation Test Sensitivity to Microstructural Evolution

After the majority of stress relaxation has taken place in the first 24 hours, irregular perturbations in stress as a function of time take place during the remainder of the test. It is possible that carbide forming elements in solution after heat treatment precipitate during stress relaxation at 760 °C since the solubility of these carbides is lower. The loss of carbon in addition to other carbide forming elements from solution likely leads to a decrease in lattice parameter of the matrix, resulting in a volume contraction. The contraction of the matrix leads to an increase in stress when the total strain in the sample is held constant in the stress relaxation test. While dilatometry would be required to prove that sample contraction takes place during relaxation, similar phenomena have been reported in several other alloy systems where volume changes and stress relaxation response are attributed to precipitate evolution [4.28–4.30]. Although these increases in stress cause some difficulty in data analysis to determine creep rate, they provide useful information about changes in microstructure during the test.

Stress relaxation testing is positioned well to accelerate creep evaluation on existing alloys and to advance alloy development by quickly screening alloys for creep strength and microstructural evolution that results in volumetric changes in the material. The more accurately that strain rate can be derived from the fitting method described herein, the better the predictions of creep rate and rupture time will be. The error in the prediction of creep rate and rupture time from the methodology described here expands as the stress being measured nears the magnitude of the stress fluctuations induced by microstructural changes, especially for large fractions of

low-stability phases and/or transformations with which a large volume change is associated. This suggests that stress relaxation tests may be best suited to predicting creep strength and rupture time for alloys with a greater degree of microstructural stability, such as low misfit γ' -strengthened Ni alloys.

4.5.3 Stress Relaxation Test Sensitivity to Differences Between Ni230 and Ni230 TiC

Both conventional creep tests and stress relaxation tests showed inferior creep resistance of PBF-LB Ni230 compared to PBF-LB Ni230 TiC. Ni230 samples showed 5× higher stress relaxation rates in Ni230 compared to Ni230 TiC within the first hour of their tests. Contributing factors for this observation include the differences in microcracking and precipitation between the two materials. This finding suggests that a < 1-hour long stress relaxation test could detect differences in creep strength, which means stress relaxation tests could be used as a quality control tool to evaluate build-to-build variations in PBF-LB processed materials.

4.5.4 Ni230 TiC Creep Behavior

It is apparent that there is good agreement between the stress relaxation predictions and conventional creep test results for Ni230, but the agreement is not as good for Ni230 TiC. As depicted in Figure 4.4, the stress exponents and creep rates derived from stress relaxation tests and conventional creep tests differ more for Ni230 TiC than for Ni230. The cause of this discrepancy may be due to the differences in microstructural evolution between the two alloys. A greater fraction of carbides form in Ni230 TiC during thermal exposure than in Ni230. The conventional creep tests show lower creep rates than stress relaxation tests indicating that increased dynamic precipitation in Ni230 TiC during primary creep increases its creep strength during conventional creep tests. The short time of the stress relaxation test does not allow for the same degree of dynamic precipitation, resulting in lower creep strength and higher creep rates as a function of stress than witnessed in conventional creep tests.

4.5.5 Considerations for Shorter Stress Relaxation Tests

While 100-hour tests were used in this study, the majority of stress relaxation takes place in the first 24 hours of the test. The utility of this is illustrated in Figure 4.8 which contains the fitted relaxation curve for the 0 % plastic strain Ni230 TiC test and the calculated creep rate. The stress decreases from 200 MPa to 52 MPa over 100 hours, but over 90 % of that relaxation takes

place in 24 hours. A 24-hour test would provide information corresponding to creep lives of over 10,000 hours based on the rupture behavior of wrought Haynes 230 at 760 °C [4.1]. An avoidable drawback of shorter stress relaxation tests is the influence of dynamic changes to the microstructure that occur at elevated temperature, such as carbide precipitation that changes creep properties. While a 24-hour stress relaxation test would fit well in a high throughput creep assessment campaign or a quality control testing setting, pre-aging and/or longer-term tests may be necessary for other applications.

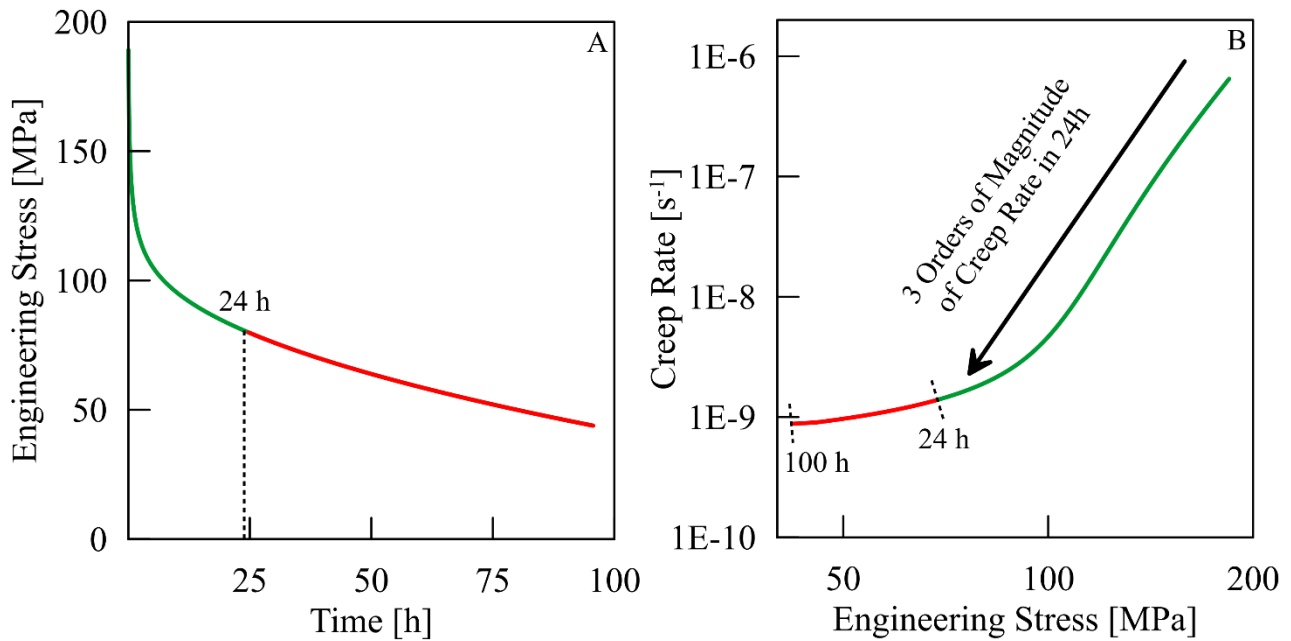


Figure 4.8. A) The relaxation observed in the first 24 hours of a stress relaxation test, and B) the range of creep rates assessed as a function of test time.

4.6 Summary and Conclusions

This work evaluated stress relaxation testing as a high throughput method to assess creep strength of a laser powder bed fusion additively manufactured version of Haynes 230 exhibiting microcracking and modified version where microcracking is eliminated. The results of a limited set of conventional creep tests were utilized to develop a Monkman Grant relation that enables the prediction of creep rupture life from the stress relaxation test results. Microstructure characterization was performed to interpret aspects of the stress relaxation test data. The following conclusions are made:

- Data from 100-hour stress relaxation tests were analyzed to evaluate creep rate as a function of stress at 760 °C resulting in creep rates as low as 10^{-9} s^{-1} .
- Stress relaxation testing was able to detect the transition from power law to diffusional creep in the finer grain size Ni230 TiC samples.
- Creep rates as a function of stress obtained from stress relaxation tests were systematically affected by the amount of plastic strain at the beginning of the test. A starting strain with no appreciable plastic deformation (at the yield point) resulted in creep rates that best matched those from conventional creep tests in the materials evaluated.
- By utilizing the Monkman-Grant relationship, rupture times were predicted from stress relaxation tests that match closely to conventional single stress creep tests.
- The poor creep performance of PBF-LB Ni230 containing microcracks compared to the modified Ni230 TiC without microcracking was easily detectible with stress relaxation testing.
- The creep performance of Ni230 TiC assessed with conventional creep testing and stress relaxation testing is comparable to wrought Haynes 230 at the conditions evaluated.
- PBF-LB Ni230 and Ni230 TiC both exhibit dynamic carbide precipitation during thermal exposure to 760 °C, leading to discrepancies between creep rates evaluated from stress relaxation testing and conventional single stress creep tests.
- Overall, there is potential for stress relaxation testing to accelerate the evaluation of creep performance in new nickel alloys, or existing nickel alloys processed in new ways (such as PBF-LB), and can contribute to more rapid alloy development for demanding structural applications.

4.7 Acknowledgements

This material is based upon work supported by the Office of Naval Research under contract No. N68335-22-C-0443. Any opinions, findings and conclusions or recommendations expressed in this material are those of the author(s) and do not necessarily reflect the views of the Office of Naval Research.

Author contributions to this work are as follows: *Daniel McConville*: Investigation, Methodology, Formal Analysis, Data Curation, Visualization, Writing – Original Draft, Writing – Review & Editing. *Ben Rafferty*: Resources, Funding Acquisition, Writing – Review &

Editing. *Kevin Eckes*: Funding Acquisition, Project Administration Writing – Review & Editing. *Stan Baldwin*: Resources, Writing – Review & Editing *Jeremy Iten*: Funding Acquisition, Project Administration, Writing – Review & Editing. *Amy Clarke*: Funding Acquisition, Writing – Review & Editing. *Jonah Klemm-Toole*: Conceptualization, Methodology, Funding Acquisition, Supervision, Writing – Review & Editing.

4.8 References

- [4.1] Haynes 230 Brochure. Haynes International, 2021. www.haynesintl.com/wp-content/uploads/2023/06/230-brochure.pdf
- [4.2] D. L. Klarstrom, H. M. Tawancy, D. E. Fluck, M. F. Rothman. A New Gas Turbine Combustor Alloy. Proceedings of the ASME 1984 International Gas Turbine Conference and Exhibit, Volume 5: Manufacturing Materials and Metallurgy, V005T11A003. 1984.
- [4.3] Z. Wu, S. R. Yarasi, J. Seo, N. Lamprinakos, A. D. Rollett. Study of the Printability, Microstructures, and Mechanical Performances of Laser Powder Bed Fusion Built Haynes 230. *Metals*, 12, 1380. 2022.
- [4.4] Y. Zhao, J. He, B. Li, Z. Gao, Q. Guo, Z. Ma, Y. Liu. The role of ceramic particles on the crack inhibition and mechanical properties improvement of Haynes 230 alloy fabricated by laser powder bed fusion. *Journal of Materials Processing Technology*, 320, 118124. 2023.
- [4.5] Q. Han, Y. Gu, J. Huang, L. Wang, K. W. Q. Low, Q. Feng, Y. Yin, R. Setchi. Selective laser melting of Hastelloy X nanocomposite: Effects of TiC reinforcement on crack elimination and strength improvement. *Composites Part B: Engineering*, 202, 108442. 2020.
- [4.6] Z. Zhang, Q. Han, S. Yang, Y. Yin, J. Gao, R. Setchi. Laser powder bed fusion of advanced submicrometer TiB₂ reinforced high-performance Ni-based composite. *Materials Science and Engineering A*, 817, 141416. 2021.
- [4.7] Z. Zhang, Q. Han, Z. Liu, X. Wang, L. Wang, X. Yang, T. Ma, Z. Gao. Influence of the TiB₂ content on the processability, microstructure and high-temperature tensile performance of a Ni-based superalloy by laser powder bed fusion. *Journal of Alloys and Compounds*, 908, 164656. 2022.
- [4.8] Y. Zhao, T. Ma, Z. Gao, Y. Feng, C. Li, Q. Guo, Z. Ma, Y. Liu, Significant reduction of grain size and texture intensity in laser powder bed fusion fabricated nickel-based superalloy by increasing constitutional supercooling. *Composites Part B: Engineering*, 266, 111040. 2023.
- [4.9] Y. Zhao, Z. Ma, L. Yu, Y. Liu. New alloy design approach to inhibiting hot cracking in laser additive manufactured nickel-based superalloys. *Acta Materialia*, 247, 118736. 2023
- [4.10] M. Muhammad, R. Ghiaasiaan, P. R. Gradl, S. Shao, N. Shamsaei. Additively manufactured Haynes 230 by laser powder directed energy deposition (LP-DED): effect of heat treatment on microstructure and tensile properties. Proceedings of the 32nd Annual International Solid Freeform Symposium, 935–947. 2021.

- [4.11] J. Veverková. Effects of Long-Term High Temperature Exposure on the Microstructure of Haynes Alloy 230. Order No. U559864, University of Leicester, England, 2010.
- [4.12] T. Tanski, M. Sroka, A. Zielinski. *Creep*. IntechOpen, 1, 19. 2018.
- [4.13] Creep Data Sheet (CDS). National Institute of Materials Science, Website: <https://cds.nims.go.jp/>. Accessed Jan. 2023.
- [4.14] K. Kim, T. Kang, M. E. Kassner, K. Son, K. Lee. High-temperature tensile and high cycle fatigue properties of inconel 625 alloy manufactured by laser powder bed fusion. *Additive Manufacturing*, 35, 101377. 2020.
- [4.15] Q. Zhong, K. Wei, Z. Lu, X. Yue, T. Ouyang, X. Zeng. High power laser powder bed fusion of Inconel 718 alloy: Effect of laser focus shift on formability, microstructure and mechanical properties. *Journal of Materials Processing Technology*, 311, 117824. 2023.
- [4.16] E. W. Hart, H. D. Solomon. Load Relaxation Studies of Polycrystalline High Purity Aluminum. *Acta Metallurgica*, 21, 295–307. 1973.
- [4.17] D. A. Woodford, D. Stiles. High-Temperature Performance Evaluation of a Directionally Solidified Nickel-Base Superalloy. *Journal of Materials Engineering and Performance*, 6, 521–533. 1997.
- [4.18] M. Manjoine, H. R. Voorhees. *Compilation of Stress Relaxation Data for Engineering Alloys*. American Society for Testing & Materials. 1982.
- [4.19] D. A. Woodford. Advances in the Use of Stress Relaxation Data for Design and Life Assessment in Combustion Turbines. *Japan Society of Mechanical Engineers International Journal*, 45, 98–103. 2002.
- [4.20] T. Cao, Z. Jie, C. Cheng, H. Li. The Application of Stress-Relaxation Test to Life Assessment of T911/T22 Weld Metal. *Journal of Materials Engineering and Performance*, 25, 1103–1108. 2016.
- [4.21] D. Tiparti, A. Wessman, J. Cormier, S. Tin. Comparison of the stress relaxation and creep behavior of conventionally forged and additively manufactured René 65. *Journal of Materials Science*. 58, 5951–5969. 2023.
- [4.22] Z. Wang, A. Stoica, D. Ma, A. Beese. Stress relaxation in a nickel-base superalloy at elevated temperatures with in situ neutron diffraction characterization: Application to additive manufacturing. *Materials Science and Engineering A*. 714, 75-83. 2018.
- [4.23] D. A. Woodford. Test methods for accelerated development, design and life assessment of high-temperature materials. *Materials and Design*, 14, 231–242. 1993.
- [4.24] F. C. Monkman, N. J. Grant. *Proc. ASTM*, 56, 593–620. 1956.
- [4.25] M. E. Kassner. *Fundamentals of Creep in Metals and Alloys*. Elsevier. 8–14. 2015.
- [4.26] F. R. Larson, J. Miller. *Transactions ASME*. 74, 765–771. 1952.
- [4.27] ASTM E328: Standard Test Methods for Stress Relaxation for Materials and Structures. ASTM International. 21. 2021.
- [4.28] S. Kinzel, J. Gabel, R. Völkl, U. Glatzel. Reasons for Volume Contraction after Long-Term Annealing of Waspaloy. *Advanced Engineering Materials*. 17, 8, 1106–1112. 2015.

- [4.29] H. Qin, Z. Bi, D. Li, R. Zhang, T. Lee, G. Feng, H. Dong, J. Du, J. Zhang. Study of precipitation-assisted stress relaxation and creep behavior during the ageing of a nickel-iron superalloy. *Materials Science and Engineering A*. 742, 493-500. 2019.
- [4.30] M. Durand, J. Cormier, P. Villechaise, J. Franchet, C. Dumont, N. Bozzolo. Metallurgical Mechanisms upon Stress Relaxation Annealing of the AD730TM Superalloy. In: *Superalloys 2020*. 546–558. 2020.
- [4.31] G. E. Dieter. *Mechanical Metallurgy*. McGraw-Hill. 2, 207. 1976.
- [4.32] L. Li, J. McCarley, E. Sun, S. Tin. Understanding the Effects of Alloys Chemistry and Microstructure on the Stress Relaxation Behavior of Ni-Based Superalloys. In: *Superalloys 2020*. 579–590. 2020.
- [4.33] B. Yang, Z. Shang, J. Ding, J. Lopez, W. Jarosinski, T. Sun, N. Richter, Y. Zhang, H. Wang, X. Zhang. Investigation of strengthening mechanisms in an additively manufactured Haynes 230 alloy. *Acta Materialia*. 222, 117404. 2022.

CHAPTER 5

CONCLUSIONS AND FUTURE WORK

5.1 Conclusions

The conclusions from this work are summarized for each research question below:

- (1) How does the creep of a modified, highly printable version of Haynes 230 compare to both the unmodified alloy processed with PBF-LB and wrought material?
 - The modified Haynes 230 showed longer rupture times and higher creep ductility than the standard alloy when creep tested with constant engineering stresses of 145 MPa, 160 MPa, and 190 MPa at 760 °C. Horizontal (XY-oriented) samples of the modified alloy showed longer rupture times compared to vertical (Z-oriented samples).
 - The modified Haynes 230 alloy showed lower minimum creep rates (higher creep strength) than standard Haynes 230, although both materials appear to be deforming in power law creep within the conditions evaluated. XY-oriented specimens exhibited lower minimum creep rates than Z-oriented specimens
 - The higher creep strength in the modified Haynes 230 alloy is likely due to a greater fraction of intergranular carbides prior to creep testing and a greater amount of dynamic precipitation during creep testing.
 - The fracture surface of standard Haynes 230 shows a large fraction of smooth features that are interpreted to be pre-existing solidification cracks in addition to some creep voids at grain boundaries. In contrast, the modified alloy shows exclusively voids that are distributed throughout the highly deformed microstructure which likely accounts for the higher creep ductility.
 - The results of a creep rupture time model suggest that the lower minimum creep rate in the modified alloy is the primary contributor to longer rupture times compared to standard Haynes 230. The finer grain size also contributes to the longer rupture time, but to a much lesser degree.

- Overall, the creep performance of the modified PBF-LB Haynes 230 is equivalent to wrought Haynes 230, and the results of this work show that existing Ni-based alloys can be tailored to improve additive manufacturability and performance for high temperature structural applications.
- (2) How well does stress relaxation testing of PBF-LB Haynes 230 predict conventional creep test results, and what are important considerations/limitations of the technique?
- By utilizing the Monkman-Grant relationship, rupture times were predicted from stress relaxation tests that match closely to conventional single stress creep tests.
 - Data from 100-hour stress relaxation tests were analyzed to evaluate creep rate as a function of stress at 760 °C resulting in creep rates as low as 10^{-9} s^{-1} .
 - Stress relaxation testing was able to detect the transition from power law to diffusional creep in the finer grain size Ni230 TiC samples.
 - Creep rates as a function of stress obtained from stress relaxation tests were systematically affected by the amount of plastic strain at the beginning of the test. A starting strain with no appreciable plastic deformation (at the yield point) resulted in creep rates that best matched those from conventional creep tests in the materials evaluated.
 - The poor creep performance of PBF-LB Ni230 containing microcracks compared to the modified Ni230 TiC without microcracking was easily detectible with stress relaxation testing.
 - The creep performance of Ni230 TiC assessed with conventional creep testing and stress relaxation testing is comparable to wrought Haynes 230 at the conditions evaluated.
 - PBF-LB Ni230 and Ni230 TiC both exhibit dynamic carbide precipitation during thermal exposure to 760 °C, leading to discrepancies between creep rates evaluated from stress relaxation testing and conventional single stress creep tests.
 - Overall, there is potential for stress relaxation testing to accelerate the evaluation of creep performance in new nickel alloys, or existing nickel alloys processed in

new ways (such as PBF-LB), and can contribute to more rapid alloy development for demanding structural applications.

5.2 Future Work

The following are possible subjects for additional exploration of PBF-LB creep and stress relaxation testing:

- To further investigate dynamic precipitation in Haynes 230 and synthesize a more comprehensive microstructural understanding, hardness testing, dilatometric studies, and X-ray diffraction would provide useful evidence to support claims on microstructural evolution during high temperature service.
- More refined analytical models can be implemented to better understand the mechanisms for improving creep strength in alloys modified for PBF-LB. These may be able to predict creep rupture time fully analytically or inform pathways for improving PBF-LB creep strength to exceed that of conventionally processed materials.
- There is ample opportunity to study more alloys with stress relaxation testing, such as γ' and γ'' precipitate strengthened Ni-based alloys, to assess the influence of microstructural stability on its creep rupture time predictive capabilities.

APPENDIX A
PERMISSIONS

[EXTERNAL] RE: TMS Publications Permission Request



Permissions <permissions@tms.org>
To Daniel McConville (Student)

Dear Daniel,

Permission is granted to include your Superalloys 2024 paper with your thesis. The original source should be noted, along with the wording "Copyright 2024 The Minerals, Metals & Materials Society. Used with permission." Please let me know if I can be of further assistance.





Best regards,

Matt Baker







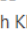

Matt Baker | Department Head, Content
The Minerals, Metals & Materials Society
5700 Corporate Drive Suite 750, Pittsburgh, PA 15237
Direct: 1-724-814-3176 | Fax: 1-724-776-3770 | Toll Free: 1-800-759-4867 (Ext. 280)
mbaker@tms.org | <http://www.tms.org>

Figure A.1. Permission granted by the TMS content department head, Matt Baker, to include the publication of "Stress Relaxation Testing as a High Throughput Method for Assessing Creep Strength in Laser Powder Bed Fusion Processed Ni-based Superalloys" from the proceedings of the Superalloys 2024 conference.

 Jonah Klemm-Toole
To  Daniel McConville (Student);  Jeremy Iten;  Ben Rafferty;  Kevin Eckes;  Clarke, Amy Jean
Tue 8/20/2024 12:15 PM

You have my permission to use our coauthored work for the content of your master's thesis

Jonah


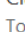
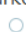

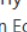
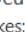

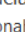
 Kevin Eckes <Kevin@elementum3d.com>
To  Jonah Klemm-Toole;  Daniel McConville (Student);  Jeremy Iten;  Ben Rafferty;  Clarke, Amy Jean
Tue 8/20/2024 12:25 PM

Hi Dan,

You have my permission to use our coauthored work for the content of your master's thesis.

Best,

Kevin Eckes, PhD | Research Scientist

 Clarke, Amy Jean <aclarke@lanl.gov>
To  Kevin Eckes;  Jonah Klemm-Toole;  Daniel McConville (Student);  Jeremy Iten;  Ben Rafferty;
 Clarke, Amy Jean;  Amy Clarke
Tue 8/20/2024 12:28 PM







[If there are problems with how this message is displayed, click here to view it in a web browser.](#)

Hi Dan,

You have my permission to use our coauthored work for the content of your master's thesis.

Thanks,

Amy

 Jeremy Iten <Jeremy@elementum3d.com>
To  Daniel McConville (Student);  Ben Rafferty;  Kevin Eckes;  Clarke, Amy Jean;  Jonah Klemm-Toole
Tue 8/20/2024 3:31 PM

[If there are problems with how this message is displayed, click here to view it in a web browser.](#)

Dan,

You have my permission to use our coauthored work for the content of your master's thesis.

Regards,

Jeremy

 Ben Rafferty <Ben@elementum3d.com>
To  Daniel McConville (Student)
Thu 8/22/2024 7:27 AM

[If there are problems with how this message is displayed, click here to view it in a web browser.](#)

Dan,

You have my permission.

Best,

Ben

Figure A.2. Permissions for the use of coauthored materials in this thesis.